Complex dynamics of small-moderate volcanic events: the example of the 2011 rhyolitic Cordón Caulle eruption, Chile

Complex dynamics of small-moderate volcanic events: the example of the 2011 rhyolitic Cordón Caulle eruption, Chile

Marco Pistolesi[(1,2)*], Raffaello Cioni[(1)], Costanza Bonadonna[(3)], Manuela Elissondo[(4)], Valerie Baumann[(4)], Antonella Bertagnini[(5)], Laura Chiari[(2)], Rafael Gonzales[(4)], Mauro Rosi[(2)], Lorella Francalanci[(1)]

[1] *Earth Sciences Department, University of Florence, Italy*

[2] *Earth Sciences Department, University of Pisa, Italy*

[3] *Earth and Environmental Sciences section, University of Geneva, Switzerland*

[4] *Servicio Geologico Minero Argentino, Buenos Aires, Argentina*

[5] *Istituto Nazionale di Geofisica e Vulcanologia, Sezione di Pisa, Italy*

*corresponding author:

Earth Sciences Department, University of Florence, via La Pira, 4, 50121, Florence, Italy

Tel. +390502215773 / Fax +390502215800

Email: pistolesi@dst.unipi.it

Abstract

After decades of repose, Puyehue-Cordón Caulle Volcano (Chile) erupted in June 2011 following a month of continuously increasing seismic activity. The eruption dispersed a large volume of rhyolitic tephra over a wide area and was characterized by complex dynamics. During the initial climactic phase of the eruption (24-30 hours on 4-5 June), 11-14 km-high plumes dispersed most of the erupted tephra eastward towards Argentina, reaching as far as the Atlantic Ocean. This first eruptive phase was followed by activity of lower intensity, leading to the development

of a complex stratigraphic sequence, mainly due to rapid shifts in wind direction and eruptive style. The resulting tephra deposits consist of thirteen main layers grouped into four units. Each layer was characterized based on its dispersal direction, sedimentological features and on the main characteristics of the juvenile fraction (texture, density, petrography, chemistry). The lowest part of the eruptive sequence (Unit I), corresponding to the tephra emitted between 4 and 5 June, is composed of alternating lapilli layers with a total estimated volume of ca. 0.75 km^3; these layers record the highest intensity phase, during which a bent-over plume dispersed tephra towards the southeast-east, with negligible up-wind sedimentation. Products emitted during 5-6 June (Unit II) signaled an abrupt shift in wind direction towards the north, leading to the deposition of a coarse ash deposit in the northern sector (ca. 0.21 km^3 in volume), followed by a resumption of easterly directed winds. A third phase (Unit III) began on 7 June and resulted in tephra deposits in the eastern sector and ballistic bombs around the vent area. A final phase (Unit IV) started after 15 June and was characterized by the emission of fine-grained white tephra from ash-charged plumes during low-level activity and the extrusion of a viscous lava flow. Timing and duration of the first eruptive phases were constrained based on comparison of the dispersal of the main tephra layers with satellite images, showing that most of the tephra was emitted during the first 72 hours of the event. The analyzed juvenile material tightly clusters within the rhyolitic field, with negligible chemical variations through the eruptive sequence. Textural observations reveal that changes in eruption intensity (and consequently in magma ascent velocity within the conduit) and complex interactions between gas-rich and gas-depleted magma portions during ascent resulted in vesicular clasts with variable degrees of shear localization, and possibly in the large heterogeneity of the juvenile material.

Introduction

Explosive activity fed by intermediate to silicic magmas spans a large range in eruptive styles and regimes, from Vulcanian to Plinian (Bursik 1993; Cioni et al. 2000; Morrissey and Mastin 2000; Houghton and Gonnerman 2008). In general, small-moderate explosive eruptions are strongly unsteady, commonly showing high-frequency oscillations in eruptive parameters, including rapid transitions in eruptive style and sharp variations in eruptive intensity (Wong and Larsen 2010). The frequency of small-moderate, VEI 3-4 eruptions is high, with global recurrence times ranging between months to a few years (Simkin and Siebert 2000). These eruptions are often associated with tephra fallout, pyroclastic density currents (PDCs) and with long-lasting phases of ash emission that often occur together with lava flow activity. The variability of the eruptive style has been commonly related to a complex interplay of different factors, such as magma supply rate, degassing style, coupling of gas and melt phases prior to and during magma rise, ascent rate of magma in the conduit, syn-eruptive bubble and microlite growth, magma rheology and fragmentation (Villemant and Boudon 1998; Cashman and Blundy 2000; Genareau et al. 2010; Adams et al. 2013). The frequent shifts in eruptive style and the long persistence of activity with low-level plumes result in complex deposits often hard to interpret. In addition, larger events associated with rhyolitic magma (which fuelled some of the Earth's largest explosive volcanic eruptions) remain poorly understood, mainly due to the lack of directly observed eruptions.

Apart from Chaitén volcano (Chile), which erupted explosively in 2008 (Castro and Dingwell 2009; Alfano et al. 2011, 2012), no important explosive rhyolitic activity was observed in the 20th Century until 2011, when Cordón Caulle Volcano (Chile) erupted after five decades of repose (Simkin and Siebert 2000). The 2011 Cordón Caulle event is an example of a subplinian to small-moderate, rhyolitic eruption (Bonadonna et al. 2015) characterized by a 24-30 hours-

long paroxysmal phase and followed by several months of low-intensity ash emissions and effusive activity. Due to the predominance of westerly winds, tephra fallout affected a wide area of Argentina and Chile and impacted both the local and regional economy, including the evacuation of 4000 people. Air traffic was disrupted by temporary closure of several Patagonian airports and flight cancellations. Agricultural economic losses were estimated at ca. USD200 million; biotic effects linked to ash deposition were also widespread (Masciocchi et al. 2013). Recent papers focused on specific aspects of the eruption (petrology, deformation history, variations in the explosive activity, mechanisms of lava flow emplacement; Collini et al. 2012; Castro et al. 2013; Schipper et al. 2013; Tuffen et al. 2013; Jay et al. 2014), but a detailed stratigraphic study of the entire eruption sequence, discussing the relative roles of intra-eruptive variability of magma physical parameters with respect to eruption dynamics parameters has hitherto been lacking. Our main objective is a field-based reconstruction of the 2011 Cordón Caulle eruption, which presents a unique opportunity to study the complex stratigraphy of a subplinian to small-moderate rhyolitic event. We also discuss possible mechanisms and parameters controlling the observed shift in eruptive activity with time.

Geological setting

The Puyehue-Cordón Caulle volcanic complex (PCCVC) is a cluster of Pleistocene to recent volcanic vents aligned along a northwest (N135°) trend oblique to the main volcanic front of the Andean Southern Volcanic Zone (SVZ; Lara et al., 2004). The PCCVC encompasses ~140 km^3 of Pleistocene and Holocene volcanic rocks that crop out over ca. 800 km^2, mainly between 800 and 2236 m above sea level (Singer et al. 2011; Fig. 1). Together with the collapse of volcanic edifices, repeated expansion and retreat of glaciers westward out of the Cordillera during the

Pleistocene (Lowell et al. 1995) reduced older parts of the PCCVC complex to erosional remnants and incised kilometer-deep valleys that culminate in Lago Puyehue in the south and Lago Ranco in the north. Puyehue stratovolcano is flat-topped in profile, reaches an elevation of 2236 m, and has a 2.5-km-diameter, 280-m deep summit caldera. Cordón Caulle, extending 20 km along a fissure zone that trends northwest from Puyehue, is covered by ca. 9 km^3 of rhyodacitic to rhyolitic domes, lava flows, pumice falls, and lahars generated from at least 27 events during late Pleistocene to historic time (Katsui and Katz 1967; Lara et al. 2004, 2006).

Two major rhyodacitic-rhyolitic fissure eruptions occurred during the 20^{th} century (1921–1922 and 1960), the latter only 38 hours after the 9.5 Mw Valdivia earthquake (the largest earthquake instrumentally recorded), centered 240 km northwest of the PCCVC (Kanamori and Cipar 1974; Moreno and Petit-Breuilh 1999; Lara et al. 2004, 2006). Tephra of the 1921–1922 and 1960 eruptions blanketed most of the central and southern sector of Cordón Caulle and the northern flank of the Puyehue stratovolcano. In addition to these major events, other minor historical fissure eruptions (VEI = 1–2) occurred in 1759, 1893, 1905, 1914, 1919, 1929, 1934 and 1990.

Chronology of the eruption

On 27 April 2011, a seismic swarm located at 4 km depth beneath PCCVC was interpreted by the Chilean Servicio Nacional de Geologia y Mineria (SERNAGEOMIN) and OVDAS (Observatorio Volcanológico de Los Andes del Sur) as caused by magma movement in the volcanic system (Collini et al. 2012). Seismic activity was persistent during May 2011, with two major events on 4 and 17 May (Mw 3.5 and 4.2, respectively). On 1 June, SERNAGEOMIN reported significant changes in volcano seismicity, with many events (750 in only 32 hours) located southeast of PCCVC at depths between 2.5 and 5 km. On 2 June the Chilean National Emergency Office

(ONEMI) changed the volcanic alert code for civil protection to yellow (level 3). In the following days seismicity increased, reaching 230–250 earthquakes per hour on 4 June, 12 with magnitude ca. 4.5 (Silva Parejas et al. 2012). ONEMI changed the volcanic alert code to red (level 5), implying imminent volcanic eruption.

The eruption started on 4 June at 14:45 local time (18:45 UTC) with the opening of a new vent and the development of a vigorous sustained eruption column that rose 10–12 km above the summit according to reports from SERNAGEOMIN, ONEMI and Buenos Aires Volcanic Ash Advisory Center (Collini et al. 2012 and Global Volcanism Program, GVP), with mass flow rate of ca. 10^7 kg/s (Bonadonna et al. 2015). The vent probably opened at the intersection of a regional lineament (the Liquiñe-Ofqui Fault) with the northern Cordón Caulle principal graben fault system, ca. 7 km north-northwest of the crater rim of Puyehue Volcano. Sustained high-rate discharge continued on the 5 June (although a bulletin released by SERNAGEOMIN at 18:00 local time of 4 June reports a general decrease of eruption intensity), when at least 5 episodes of partial column collapse occurred, generating PDCs mainly heading north. From 5 to 7 June the plume height started to fluctuate between 12 and 8 km high. On the 6 June plume dispersal rapidly shifted counterclockwise, heading NNE, before being again dispersed by westerly winds in the morning of the 7 June. The volcanic cloud reached the Atlantic coast early on 5 June, turning northeast to reach northern Argentina on 7 June and Buenos Aires on 9 June. After the peak in intensity of 4 June, until 15 June the column height fluctuated with mass flow rate always $>10^6$ kg/s (Bonadonna et al. 2015), and a number of PDCs were also reported.

During this period, the fine-grained ash fraction was continuously injected into the atmosphere, circling the Southern Hemisphere, passing over southern Australia on 10 June, reaching the southern tip of New Zealand on 11 June, and returning to South America on 15 June, completing its first circle of the globe by 18 June. Seismic events diminished progressively from

17 to 5 earthquakes per hour. After 16 June, seismicity changed to low-frequency harmonic tremor, and the eruption column height was around 3 km. This change possibly accompanied the ascent to the surface of a magma body, anticipating the emission of viscous lava that was first observed on 20 June (Tuffen et al. 2013). According to SERNAGEOMIN, the end of the effusive phase during the first months of 2013 closed the eruption.

Methodology

Four field campaigns were conducted to characterize the eruption deposit stratigraphy (Fig. 1A and B), with the first observations just a few hours after the onset of the eruption; other detailed stratigraphic and sampling surveys were conducted during July 2011 (when the eruption was still ongoing), November 2011, May 2012, and February 2013. We investigated about 70 outcrops from proximal (1 km) to distal (240 km) areas to define the complex stratigraphic architecture of the tephra deposits, and to unravel the time-related variability of erupted products. Deposits were also studied for their sedimentological, physical (volume, grain-size, componentry, density), textural and chemical characteristics. The tephra sequence was correlated among the different outcrops, and a detailed comparison with satellite imagery allowed a precise timing of the eruptive phases to be reconstructed.

At each site, a detailed stratigraphic log of tephra layers was measured and described. The tephra sequence was mainly investigated in the northeastern and southeastern sectors, where most of the tephra was dispersed during the initial intense phases of the eruption (Fig. 1). Thin deposits were also recognized NNW of the eruptive vent, upwind of the main dispersal axis of the tephra fallout. Based mainly on sedimentologic features (color, grain-size, size grading of deposits), the tephra sequence was subdivided into layers that represent single eruptive pulses. The layers were organized into units (based on abrupt changes of lithological and granulometric

167 features) representing different stages of the eruption sequence. Several key sections located
168 along the dispersal axis (vent area, Río Gol Gol, Paso Cardenal Samoré, Lago Espejo, Villa La
169 Angostura, Bariloche, Ingeniero Jacobacci (1 to 7, respectively, in Fig. 1A) were particularly
170 useful to trace correlations between different tephra layers and to reconstruct an "ideal"
171 stratigraphic sequence that comprises all the products emplaced during the first weeks of the
172 eruption. Field thickness data were hand-contoured onto isopach maps (4 to 7 contour lines,
173 from 0.1 to 30 cm). Dispersal maps of the different layers were compared with all available
174 satellite images of the plumes dispersed during the different eruption phases and the resulting
175 deposits. In particular, we used NASA MODIS (Moderate Resolution Imaging
176 Spectroradiometer) Terra and Aqua and NOAA GOES (Geostationary Satellites) images for the
177 period 4-9 June (a minimum of 5 images were used for each analyzed day). At some selected
178 key sections, tephra deposits were also sampled for grain-size analyses. Samples were
179 mechanically dry-sieved at half-ϕ intervals (ϕ=-$\log_2$D, where D is the particle diameter in
180 millimeters) for the coarser fraction and then processed for fine material (<0.25 mm) with a
181 laser-diffraction instrument (CILAS 1180). The combination of sieving and laser-diffraction data
182 was validated on selected samples by overlapping data resulting from the two techniques for
183 the fractions between 0.5 and 0.063 mm; grain-size parameters were calculated according to
184 Inman (1952) and Folk and Ward (1957). The coarse fraction from the key sections (≥1 mm,
185 which is ≥40-50 wt.% in each sample) was analyzed for componentry; components from each
186 grain-size class were separated by hand picking under a binocular microscope and weighed.
187 Different clast types were also described in thin sections and with back-scattered mode (BSE)
188 scanning electron microscope (SEM) observations. Chemical analyses were performed on
189 powdered aliquots of vesicular lapilli from selected layers of all the main coarse-grained units
190 by inductively coupled plasma mass spectrometry (ICP-MS) at ALS Laboratories (Seville, Spain).

Density measurements of juvenile clasts from a subset of the same units were performed on vesicular fragments from a restricted size fraction (-3<ϕ<-2) collected from the tephra deposit at key sections 2 (15 km SSE of the vent) and 3 (28 km), following the method of Houghton and Wilson (1989) by determining weights in air and water after sealing. Clast densities were converted to vesicularity values by using a dense rock equivalent (DRE) measured with a water pycnometer on powders obtained by grinding the same clasts. The density of juvenile fragments as a function of grain-size was also measured for clasts from 3 layers collected at section 2. Density of clasts from -4 to -1ϕ was determined with the method of Houghton and Wilson (1989); for grain-size from -1 to 1ϕ, an aliquot (around 2 g) of juvenile clasts for each size fraction was sealed with silicon spray and the cumulative volume measured on a high-precision balance (10^{-6} g) with a 50 ml pycnometer, using distilled and degassed water and following the method of Eychenne and Le Pennec (2012).

Stratigraphy

Architecture of the tephra deposits

Thirteen layers grouped in four different tephra units were identified within the eruptive sequence and correlated among all the surveyed stratigraphic sections. Correlations in proximal and medial outcrops were carried out based on lithology and grain-size characteristics at the outcrop scale. Within 25 km from the vent, the sequence is dominated by multiple lapilli-bearing fallout layers (Units I and II) overlain by cm-thick, light gray, ash-rich fallout layers (Unit III). In the most proximal outcrops, along the slopes of the PCCVC, a fourth (younger) unit can also be recognized (Unit IV), represented by very fine-grained, thin (few millimeters to 1-2 cm) white ash. At outcrops 25 to 50 km from the vent, the sequence appears as a stratified, fine lapilli-bearing, multiple deposit (Units I and II), capped by multiple fine ash layers interbedded

with thin, coarse ash to fine lapilli beds (Unit III). At very distal outcrops (>200 km), the whole eruptive sequence is recorded by multiple beds of gray to white fine ash.

Thickness of different layers at each outcrop, grain-size parameters and componentry of representative samples are reported in Tables 1 and ESM1.

Unit I (Layers A to F)

Unit I (Fig. 2B) is a lapilli-bearing bedset made of six layers (A to F) which comprises the coarsest deposits of the eruption. It is mainly composed of pumice clasts, ranging in color from white at the base to yellow in the upper two-thirds of the unit. It is characterized by a distinct, multiple reverse grading, with three main coarser layers (B, D, F). The different layers of Unit I are separated by planar surfaces defined by sharp grain-size variations at many proximal (<25 km) outcrops (Fig. 2A and B); farther from vent (25-50 km), separation between the six layers becomes speculative (Fig. 3A), and the deposit grades into a single thin (<10 cm), massive, fine lapilli to coarse ash bed (Fig. 3B, C). Only the doublet formed by the A-B layers can be consistently distinguished among the deposits of Unit I within the first 50 km from the vent. The A-B doublet is made of highly vesicular, white pumice clasts, and the two layers progressively merge away from the vent into a single, reversely graded bed dispersed to the southeast, and always associated with the deposits of the following layers of Unit I (C to F); these in turn cannot be unequivocally separated farther than 20-25 km from the vent and are characterized by the coexistence of white and yellowish pumice clasts of the same composition, with the topmost part of Unit I, corresponding to layer F, being coarser-grained than the rest of the layers.

At section 7 (Fig. 1, 240 km from the vent), the Unit I deposit, collected on a tombstone relatively sheltered from winds, consists of a uniform fine ash layer (Figs. 3D and 4). In transects

238 across the dispersal area, Unit I rapidly thins and is commonly absent towards the north
239 (sections 8, 9 and 13; Fig. 4), where Unit II was directly deposited on the soil.

240 *Unit II (Layers G and H)*

241 Unit II comprises the two lapilli-bearing layers G and H and is clearly exposed in the
242 northeastern sector. Layer G has been observed in the very proximal area around the vent
243 (section 1; Figs. 4, 5B), where it consists of a 4 cm-thick, dark, poorly sorted coarse ash deposit,
244 mainly made up of white pumice clasts and abundant obsidian chips, similar to those
245 sporadically found in the other layers. It is mainly dispersed toward the north-northeast and is
246 found sandwiched between Unit I and layer H deposits along the first 10 km of the road from
247 Villa la Angostura to San Martin de Los Andes, which runs roughly parallel to the Argentina-
248 Chile border (Fig. 1B), 40 km east of the vent. At this distance, the layer is represented by a 1
249 cm-thick, obsidian-rich ash bed. Farther north, layer G is found directly on soil and is the only
250 deposit of Unit II in that area (section 9; Fig. 4).

251 Due to the NNE dispersal of layer G, Unit II is represented in most of the outcrops of the
252 eastern sector only by layer H, which clearly separates the deposits of Units I from those of Unit
253 III. Layer H is a thin, normally graded layer of fine pumice lapilli characterized by the coexisting
254 light gray and light brown-orange clasts (Fig. 2C and D). At section 5 (48 km from the vent),
255 layer H consists of a basal, 1 cm-thick, lithic-rich, coarse-grained ash deposit with a light brown-
256 orange color overlain by a gray, finer-grained, normally graded, 3 cm-thick ash layer. Within the
257 tephra sequence deposited at section 7 (240 km from the vent; Figs. 3D and 4), H corresponds
258 to a 1-mm-thick orange ash layer separating Units I and III. Due to its distinctive lithology, layer
259 H is a useful marker bed for reconstructing the complex stratigraphy of the deposits.

260 *Unit III (Layers K)*

Unit III is composed proximally of five layers (K1 to K5), easily identifiable by their different grain-sizes; main divisions were made using the ubiquitous coarser (fine-lapilli) grain-size of layer K2 and, although less frequently recognized in the field, of K4. Conversely, layers K1 and K3 are finer-grained than K2 and K4 and show multiple internal laminations. Partial erosion or wind reworking often affected layer K5. In both medial and distal areas, Unit III is easily recognized at the top of the tephra sequence by the abrupt color change to light gray from the darker A-F layers (Unit I) below.

In transects across the main dispersal axis, and at larger distances from the vent (e.g. sections 8, 9, 12; Figs. 3D and 4), the distal tephra sequence consistently contains the trace of the different layers forming Unit III, with K2 the easiest to identify by its coarser grain-size. In some proximal outcrops, snow intercalations between tephra layers of Units I and III were also observed during the first survey (Fig. 3C), possibly suggesting low accumulation rates for some beds and/or small pauses between eruptive phases.

Unit IV

Unit IV is a white, millimetres-thick fine ash deposit (layer L) which caps the whole sequence in very proximal outcrops and is present as a thin sprinkling on the southern slopes of Puyehue volcano and in a few outcrops within a radius of 20 km from the active vent. Due to its limited dispersal coupled with partial reworking, Unit IV was not used for correlation of tephra layers. In very proximal outcrops, up-wind tephra deposits corresponding to Units I to III, are covered by the generally thin, discontinuous ash of Unit IV. The grain-size of this ash does not vary significantly with distance from the vent, suggesting deposition from ash-rich plumes during low-intensity activity.

Near-vent deposits

285 Observations carried out in proximal areas revealed very limited up-wind sedimentation during
286 the entire explosive phase. Although the wind direction changed during the eruption, proximal
287 up-wind tephra deposits are restricted to a narrow, 2 km-wide, north-south area on the
288 western part of the vent. A 50 m-high tephra cone formed during the first days of the eruption
289 (Schipper et al. 2013), which was partially opened on the northwestern side and surrounded by
290 a thick lava flow during the following weeks of activity (Fig. 5A). Tephra deposits rapidly thin,
291 disappearing 1 km west of the vent; in this area (section 1; Fig. 4), the lower part of the tephra
292 sequence consists of a 5 cm-thick basal deposit of vesicular lapilli in a muddy brown ash matrix
293 (Unit I; Fig. 5B). The different layers of Unit I identified in the medial outcrops cannot be
294 distinguished. Unit I is overlain by a 3.5 cm-thick, dark-colored ash deposit rich in obsidian chips
295 (layer G, Unit II). The top of the sequence is a 3 cm-thick, gray, fine ash with dark, coarse,
296 interbedded ash laminae (Unit III).
297 The proximal area hosts many ballistic blocks, clearly visible in satellite images. Fields of metre-
298 sized bombs and blocks with related impact craters are concentrated on the northern side of
299 the cone (Fig. 6A) (see also Castro et al. 2013). The density of impact craters per unit area,
300 extrapolated from high-resolution NASA Modis and Google Earth satellite images, is 14200/km^2
301 at 1.4 km from the vent and rapidly decreases to 2400/km^2 at 2.3 km from the vent (Fig. 6B).
302 These numbers are a cumulative estimate over the whole eruption. We directly observed a field
303 of ballistic blocks 1800 m from the vent, where impact craters reached 7 m in diameter. Ballistic
304 material varies from highly vesicular to dense; dense blocks generally correspond to sub-
305 angular pieces of glassy, sometimes sparsely banded obsidian, while bombs show a large
306 lithologic variability. At least three different end-member bombs were recognized:

307- - black, glassy-rinded bombs, with highly vesicular inner portions and breadcrusted external
308 surfaces (Fig. 5C); vesicle shape and size range widely, and vesicles are sparsely distributed in
309 the bombs, often coalescing in the core to decametric size.
310- - scoriaceous, banded, bombs characterized by a range in vesicularity corresponding to light
311 colored or dark colored bands (Fig. 5D); in some cases these bombs also have a dense, glassy
312 rind;
313- - bombs formed by spectacularly welded, highly contorted, breccia-like material (Fig. 5E). The
314 breccia material is generally formed by centimetric to decimetric angular pumice, grey to pink
315 colored clasts commonly separated by a finer-grained (cm- to mm-sized) matrix of the same
316 material. Some clasts in the matrix are deformed and oriented. These bombs contain large gas
317 cavities (up to 20 cm).
318 All ballistic blocks and bombs clearly deformed layer G upon impact and, therefore, were
319 presumably ejected during phase K1-2. Ballistic ejection possibly also accompanied the later
320 phases of the eruption, which were characterized by a lower intensity than that of the first 10
321 days of activity (Bonadonna et al. 2015) and the formation of low altitude ash plumes.
322 SERNAGEOMIN and OVDAS reported an intense phase of ballistic ejection on 12-13 June
323 (before the onset of the effusive activity), when jets of pyroclastic material carrying large blocks
324 to distances up to 2.5 km were associated with oscillating tremor signals and seismic peaks
325 (Schipper et al. 2013).
326 Although it was not possible for us to directly observe PDC deposits in the field, high-resolution
327 satellite images allowed a good definition of their boundaries and some distinctive features.
328 Satellite images show large areas with trees knocked down and aligned along the main flow
329 direction, bordered by areas with still standing, partially burned trees; analysis of these images
330 revealed that most of the deposits were emplaced in valleys heading north from Cordón Caulle,

as also shown by pictures of the eruption taken on 4 and 5 June. Due to topographic effects, some flows were channelized within the main valleys, while others reached topographic highs. The total area covered by the PDC deposits is estimated at 87 km^2 (Fig. 6C), for a total runout of 12 km, and is characterized by fallen trees in different directions (Fig. 6D), suggesting that multiple flow lobes were emplaced in the same area. Assuming an average thickness $\leq$1 m (trunks of downed trees are still visible and not fully covered by the ash), we obtain a total volume for the PDC deposits of 0.08±0.01 km^3 (by considering an average error of 10% both on area and thickness estimates of the deposit).

Timing, dispersal and volume of tephra layers

Satellite images showed that, during the first hours of the eruption (4 June) and at least until 5 June, the volcanic cloud was dispersed towards the east-southeast (Fig. 7, Table 2). During the night of 5-6 June (more than 30 hours after eruption onset), the volcanic cloud drifted rapidly north due to a change in wind direction and remained stable for the entire day. A second change in wind direction occurred early on 7 June, causing the cloud to rotate back again towards the east, with minor shifting continuing until 8 June. The plume was continuous, although progressively decreasing in height, until 7 June. Starting on 8 June, the trace of the cloud on the satellite images became narrower and strongly stretched, suggesting a progressive decrease in eruption intensity, with wind velocities ranging between 30 and 60 m/s.

Comparison of deposit dispersal with satellite images constrains the timing of the different phases of the event. The coarser-grained layers A-F (Unit I) were related to the first 24-30 hours of the eruption (afternoon of 4 to morning of 5 June). Layer G, mainly dispersed to the north, was deposited overnight between 5 and 6 June while the plume drifted north along the Chile-Argentina border. After a new shift in wind direction, layer H was emplaced starting on the

night of 6 June. A pause of a few hours followed before the emplacement of layers K (Unit III), as also evidenced by snow intercalations within the tephra sequence. The vesicular aspect of the ash beds and the local occurrence of accretionary lapilli in layer K1 close to key section 5, coupled with direct observations during the eruption in Villa La Angostura describing the fallout of a muddy rain (personal communications from residents), indicate that K1 was emplaced during the late night of 6-7 June. A shower of coarser lapilli, representing layer K2, fell on the morning of 7 June, as also suggested by direct observations. The K3 and K4 ash layers were possibly emplaced immediately after K2 (8-9 June) or are either related to activity after 10 June. The eruptive activity after the first week did not form distinct beds in the distal sectors, but it was responsible for depositing the white ash of Unit IV all around the volcano at proximal sites (<20 km).

Isopach maps (Fig. 8) show that the very first phase of the event, represented by layers A and B, has a more limited dispersal than the following layers and is restricted to the first 60-70 km from the vent. Layers H and K2 layers have an intermediate, east-oriented dispersal, if compared with A-F, which covers the largest area reaching Ingeniero Jacobacci (240 km from the vent) with the 0.5 cm contour line. A-F isopachs and A-B and H at a lesser extent, show an asymmetric distribution (with the isopachs spreading more northeasterly than southwesterly) possibly due to the wind rotation during the first phase (Table 2) that progressively developed a fan towards the northern quadrants.

The erupted volume was calculated for layers A-B, A-F, H and K2, the layers most easily correlated in the field. In order to quantify uncertainty, we have applied main existing strategies (i.e., integration of exponential, power law and Weibull fit; Pyle 1989; Bonadonna and Houghton 2005; Bonadonna and Costa 2012) (Fig. 9 and Table 3). All strategies agree well with each other except for A-F, for which the exponential fits (two or three segments) give

values lower than power law or Weibull methods (from 0.44 to 0.88 km^3). Based on the average among the different methods, we obtained a volume of 0.21 km^3 for layers A-B, representing the very first stage of the eruption, of 0.75 km^3 for the whole A-F, and of 0.21 and 0.05 km^3 for layers H (Unit II) and K2 (Unit III), respectively. The volume of the post-7 June 2011 deposit could not be calculated due to correlation and erosion problems, but it is expected to be of significantly lower magnitude. Volume estimate of PDCs corresponds to ca. 10% of the A-F (average) total volume, suggesting that most of the magma volume fueled the eruptive column.

Physical features of the erupted material

Field observations were integrated with grain-size and componentry analyses (in the range -5ϕ to 0ϕ), and density, vesicularity and bulk rock chemistry of the juvenile vesicular material in order to characterize the physical and chemical features of the erupted material and their variations. We particularly focused on variations with time of the eruptive products, in order to discuss the relationships between heterogeneities in erupted materials and observed variations in the eruptive style and dynamics.

Grain-size and componentry

Five sections (1, 2, 3, 5 and 7) were selected to investigate grain-size and componentry variations within the eruptive sequence. The sections are located 1, 15, 28, 48 and 240 km from the vent, respectively (Figs. 1 and 4).

Proximal outcrops (sections 2 and 3) have similar vertical variations in grain-size, showing oscillations in the median grain-size of the deposits of Unit I (Figs. 10 and 11; Table 1). Unit I is also characterized by good sorting ($\sigma\phi$ between 1.16 and 1.72). Units II and III show an abrupt

decrease of grain-size with respect to Unit I. Section 1, 1 km upwind of the vent, is characterized by a rapid upward decrease in mean grain-size and sorting passing from Unit I to Unit II, represented by layer G (Fig. 12).

The tephra sequence at medial outcrops (e.g. section 5; Villa La Angostura, Fig. 12) is also characterized by a clear grain-size difference in the deposits, with a coarser basal bed corresponding to Unit I (in which the different sublayers recognized in the more proximal area are here represented by a single, lapilli-bearing bed) overlain by finer-grained Units II and III. The layers of Unit III (Fig. 12) show a very clear bimodality of grain-size, with the coarsest layer (K2) more enriched in the coarse population (with a mode around -0.4ϕ) with respect to the K1 and K3-5 layers. Units I and II are well to very well sorted whereas Unit III is poorly sorted (Table 1).

Analyses performed on the distal tephra sequence (section 7; Ingeniero Jacobacci, Fig. 12) show a very fine uniform Mdϕ (5.3-5.5) and are well sorted ($\sigma\phi$=1.5-1.6). Samples are characterized by F2>74% (where F2 represents the wt.% of ash fraction <63 μm).

In general, all samples of the lower three units present a clearly bimodal grain-size distribution, particularly evident in Units II and III (Bonadonna et al. submitted). A finer-grained mode generally peaks between 3ϕ and 5ϕ in all the samples, while the coarsest fraction has a mode that strongly varies according to the distance from the vent and the position of the deposit with respect to the dispersal axis (Table 1).

Component analysis of the deposits was conducted on the coarsest (≥1 mm) grain-size fraction of samples from four stratigraphic sections at different distances from the vent, along the main dispersal axis of the deposit (sections 1, 2, 3 and 5). Componentry data are presented in Table 1. On the basis of macroscopic external morphologies, texture, degree of alteration, crystallinity and vesicularity, we separate juvenile and lithic clasts. Observations of thin sections, coupled

with SEM imaging, of the material reveal a large range of juvenile lithology, which can be subdivided into five different types: i) white pumice clasts, ii) banded pumice clasts, iii) dense juvenile clasts, iv) obsidians and v) free crystals (Fig. 13):

- *white pumice clasts*: highly vesicular, nearly aphyric clasts. Vesicles have wide range in shape (from spherical, to irregular, to convoluted, to tubular) and size. Some clasts shows fluidal structures, marked by highly deformed, convoluted vesicles. Rare phenocrysts of plagioclase and pyroxene are present, generally oriented along the fluidal structures defined by the largest vesicles. Glomeroporphyritic textures (pyroxene and plagioclase) are also observed. Important differences in the general shape of vesicles (and consequently of the clasts) are observed between samples of lapilli-bearing layers (A-F, H, K2 and K4) and samples from layers characterized by an abundant ash component even in the proximal sectors (G, K1, K3, K5, Unit IV). In the ash-rich layers, elongated pumice clasts with tubular vesicles coupled with dense clasts with collapsed vesicles dominate in the fine lapilli to coarse ash component, while in the lapilli-bearing layers both the lapilli and coarse ash components are dominated by the presence of subequant fragments with spherical to deformed, convoluted vesicles.
- *Banded pumice clasts*: fluidal, poorly to moderately vesicular, subaphyric clasts, characterized by alternating light and dark grey bands (banded or streaky pumice). These clasts are generally fine-grained (ϕ>-2). Many vesicles are elongated; light colored portions are generally more vesicular. Macroscopically, banded pumice resembles the ballistic scoriaceous banded bombs observed in proximal area.
- *Obsidian clasts*: black to transparent brown, dense, massive to fluidal, subaphyric glassy fragments, with vitreous luster. Microlites are rare, and if present show a skeletal texture. In thin section the color of the glass ranges from light yellow to brownish. The darker

fragments are characterized by a weak color banding. While fresh, vitreous clasts possibly represent juvenile material, dull black fragments could derive from the shattering of preexisting obsidian bodies (accidental lithics). Obsidian fragments are particularly abundant in the G layer, although they are present in variable amounts throughout the whole sequence. This type of clast is generally found only in the coarse ash fraction.

- *Dense juvenile clasts*: aphyric to subaphyric, poorly vesicular, glassy grey fragments. Vesicles are small and generally spherical. In thin section the glass is transparent and unaltered, with very few microlites and no trace of banding or fluidal structures. Phenocrysts are plagioclase and pyroxene. These clasts have intermediate features between banded pumice and obsidian fragments.
- *Free crystals*: millimetric to sub-millimetric crystals of plagioclase and rare pyroxene. Crystals are commonly present as fine-grained aggregates of subhedral plagioclase and pyroxene with interstitial glass and microlites of oxides.

Lithic material is more homogenous than the juvenile clasts, and two different lithologies were distinguished:

- *altered clasts*: fragments of igneous and sedimentary rocks with pervasive alteration (mainly oxidation) which conceals the original texture of the rock, making lithological recognition very difficult. Lava fragments are sometimes recognized by their scoriaceous texture or the presence of fairly abundant plagioclase and pyroxene crystals; accessory pumice (not juvenile) can be recognized by the occurrence of hydrothermally altered ash filling the vesicles.
- *Intrusive rocks*: dark grey, fine-grained, holocrystalline fragments. In thin section these clasts present a typical monzogranite paragenesis, and a high temperature alteration paragenesis

(sericite plus epidote). Due to the small amount of intrusive rocks, lithics are treated in the following as a single category.

Componentry variations within the tephra sequence of sections 2 and 3 (Figs. 10, 11) show that, within Unit I, white pumice clasts are the most represented category (72 to 93 wt.%), followed by lithic clasts (5-25 wt.%, most abundant in layers C and F) and minor obsidian, banded pumice and dense juvenile clasts (<5 wt.%). Banded pumice clasts tend to increase from base to top of Unit I, and account for up to 9 wt.% in layer F at section 2 (Figs. 10, 11; Table 1).

Unit II is more variable, with layers G and H having contrasting componentry. At section 2, only layer H is present, consisting of abundant white pumice clasts, minor banded pumice clasts, scarce lithic fragments and virtually no dense juveniles. The characteristic reddish color of part of the white pumice fraction (in general concentrated in a thin bed at the base of the layer) is related to external oxidation of the glass. Layer G, present only in the most proximal sites (section 1) and in a narrow lobe trending NNE, is instead characterized by abundant obsidian fragments (ca. 30 wt.%) and by white pumice with elongated, tube-like shapes, rare in the underlying layers. Unit III is characterized by an abrupt change in the color of the pumice clasts from white to light gray, a clear increase in banded pumice clasts (2-8 wt.%) and the virtual absence of lithic material (<1 wt.%). As a general rule, the coarsest grain-sizes are formed only by white pumice fragments, while lithic clasts and the other types of juvenile material are present in grain-size classes with ϕ between -2.5 and 0. Free crystals are more abundant in the 0ϕ class. White pumice in the ash-bearing layers of the unit (K1, K3, K5) is typically present as tube-like fragments.

Componentry analyses performed at medial distances (section 5) show no systematic variations for Unit I, and an abrupt increase in banded and dense juvenile clasts within K layers. Layer K2, in particular, consists of abundant white pumice clasts (84 wt.%), banded pumice clasts (9 wt.%)

and free crystals (2 wt.%), with virtually no dense juvenile or lithic clasts. Layer G, analyzed only at section 1, is very rich in obsidian (27 wt.%) and dense juvenile clasts (12 wt.%) (Fig. 12).

Density

Density was measured on 80-100 white pumice clasts in the size range 2-4 cm collected from each of the coarsest layers of Unit I (B, D and F) at section 3 (28 km from the vent), from Unit II (layer H), and Unit III (layer K2) at section 2 (15 km from the vent). Density distributions show unimodal trends, with values ranging from about 200 to 1000 kg/m^3 (mean value = 485±141 kg/m^3), corresponding to vesicularities of 62 to 92 vol.% (Fig. 14A). Vesicularity trends (calculated using a measured dense rock equivalent (DRE) density of 2690 kg/m^3) show no systematic variations within Unit I (83.3±4, 83.7±3, 83.8±3 average vol.% for layers B, D and F, respectively), whereas a decrease can be observed for the younger Units II and III (78.5±6 and 77.0±5 average vol.% for H and K2, respectively).

The variation of clast density with grain-size was evaluated for layers C, F and K2 collected at section 3. The data have a sigmoidal distribution (Fig. 14B), as also observed by Eychenne and Le Pennec (2012) for the August 2006 Tungurahua subplinian scoria layer (Ecuador). Density values are similar in the -4 to -3ϕ range, with a rapid increase below -3ϕ. The trends do not reach a well-defined plateau, with maximum values of 1270 kg/m^3 for the finest (1ϕ) class, well below the measured DRE values (2690 kg/m^3), suggesting a rapid increase in density in the range 2-5ϕ. Density values are practically the same for the three samples down to -1ϕ but diverge at finer grain-size classes in the K2 sample, suggesting a different distribution of vesicle size in the clasts from Unit I compared with those from Unit III.

Vesicle shape in pumice clasts

521 Vesicular white pumice clasts have a very complex distribution of vesicles, well evident in thin
522 sections. White pumice fragments from all layers of Unit I, and from lapilli-dominated layers of
523 Unit II (layer F) and III (layers K2 and K4) show both spherical, homogeneously distributed
524 vesicles and complex, very contorted vesicles (Fig. 15A, B). Tubular vesicles occur, but they are
525 generally discontinuous, commonly affected by convolutions which deform and interrupt the
526 vesicle tubes. When observed in polished sections with the SEM, white pumice clasts present
527 clear evidence of shear localization, with obvious shear bands interrupted by transverse rigid
528 and plastic structures generally oriented at high angles with the shear bands (Fig. 15C, D). Some
529 structures resemble Riedel fractures or CS foliations. Many zones of shear localization insulate
530 areas where deformation is not evident and vesicles are homogeneous in size and nearly
531 spherical (indicated by lines in Fig. 15E, F). The overall arrangement of vesicles in these clasts
532 indicates relatively low large bubble connectivity, as strained vesicles are generally interrupted
533 over a short length by the occurrence of transversely-oriented structures.
534 Conversely, vesicular pumice clasts from ash-dominated layers (layer G of Unit II, ash-bearing
535 layers of Unit III, Unit IV) are mostly characterized by elongated shapes, owing to the
536 occurrence of very well developed tubular vesicularity or clear vesicle collapse (Fig. 15G, H). In
537 these fragments, vesicle trains are nearly parallel and not interrupted by transverse structures,
538 evidence of the development of flow banding without important shear localization and
539 deformation under a lower shear rate relative to those described for Unit I.
540

541 ## Chemistry

542 Bulk rock analyses were performed on white pumice clasts from selected layers of key section 3
543 for A to F layers, from key section 4 for layer K2, and from bombs sampled close to the crater
544 area at section 056 (Table ESM2). Major-element values for most samples cluster in a narrow

545 range within the rhyolitic field on a total alkali vs. silica plot (Le Bas et al. 1986), as described by
546 Castro et al. (2013) and Daga et al. (2014); exceptions are layers B and C, whose compositions
547 lie along the rhyolite-dacite boundary. All samples are tightly clustered between 68.51 (layer C)
548 and 71.6 (layer K2) wt.% SiO_2, with a small variability for layer D and K2, which show a slightly
549 more evolved composition. The slight change in silica content is not accompanied by an
550 increase in phenocryst content or groundmass crystallinity as shown by petrographic
551 observations; it could be related to incorporation of glomeroporphyritic clots often present
552 within the pumice clasts.
553 Trace elements show that the basal part of the tephra sequence (layers A and B) is
554 characterized by a less evolved signature, as shown by Sr and Th concentrations (Fig. 10). Plots
555 of Th vs. other elements (Cs, U, La, Ba) show positive correlations for most of the samples;
556 however, samples belonging to the topmost part of the eruptive sequence (layers E, F and K2)
557 lower Cs, U, La and Ba with respect to their higher Th contents. In general, these small changes
558 probably did not influence variations in dynamic and rheologic parameters controlling the
559 eruption, though they might reflect complex processes of magma evolution before eruption.
560

561 ## Discussion

562 The 2011 eruption of Puyehue-Cordón Caulle was fed by the ascent of slightly porphyritic,
563 rhyolitic magma from a relatively shallow (ca. 5 km) depth (Castro et al. 2013; Schipper et al.
564 2013). Although we identify several juvenile components, most is nearly homogenous rhyolitic
565 white pumice clasts containing approximately 70 wt.% SiO_2 with only minor variations in trace
566 element composition. We constrain the stratigraphy, dispersal and volume of the eruptive
567 phases and the timing by comparing deposit dispersal with satellite images. Insights into

568 temporal variation of eruption dynamics before the effusive phase derive from changes of
569 sedimentological, chemical and textural features of the explosive deposits.
570
571 ## Insights into eruption dynamics from deposit characteristics
572 Grain-size and dispersal of the tephra deposits and comparison with plume direction observed
573 by satellite images suggest that Unit I was emplaced during the first 24-30 hours of the eruption
574 (4 and 5 June) under nearly stable wind conditions. Despite this, the column clearly resulted
575 from pulsating, unsteady magma discharge, as shown by some videos taken on 4 and 5 June
576 (http://www.youtube.com/watch?v=1ulakwwtoUg; http://vimeo.com/24715989;
577 http://cimss.ssec.wisc.edu/goes/blog/archives/8281). Such unsteady discharge probably
578 resulted in the oscillating vertical grading of the fallout deposits A-F. In addition, several
579 episodes of partial column collapse-generated PDCs during the first days of the eruption (at
580 least 5 in the first two days) are recorded in the daily bulletins issued by the Chilean OVDAS.
581 Despite these oscillations, during this phase the plume was continuously supplied and the slow
582 change in wind direction from NW to W forced all the eruptive cloud to drift in W-E direction.
583 Deposits of Unit II (layers G-H) signal a change in the eruption dynamics. Satellite images show
584 narrower, less dense plumes after the morning of 6 June, possibly related to a lower mass
585 discharge which resulted in the detachment of the plume in different pulses. During the
586 deposition of Unit II, significant changes in column height and plume direction also occurred.
587 Rotation of the dispersal axis occurred during the night of 5-6 June, and the plume remained
588 stable toward the NE until the following day, leading to a gap of tephra deposition in the
589 eastern sector. The NE dispersed eruption cloud was sharply diverted to SE at a distance of
590 about 1000 km NE from the vent, where it encountered a different wind field which caused the

591 formation of a prominent “elbow” in the plume (Fig. 7C). The fine-grained, obsidian-rich, ash-
592 bearing layer G was only dispersed to the northern sector, thus representing the combined
593 result of a decreased intensity of the eruption and of the progressive shift from westerly to
594 southerly winds. The different lithology of layer G with respect to the deposits of the preceding
595 phase (large amount of juvenile obsidian clasts, finer-grained nature of the deposit) also
596 indicates that important changes in the eruption dynamics and/or a possible shift in vent
597 location had occurred. These changes anticipate and prepare for the shift towards a phase
598 dominated mainly by ash emission, generation of low-level plumes and pulsating activity,
599 recorded by the deposits of Unit III and by the wide ballistic bomb field in the proximal area.
600 Before passing to this phase, however, the eruption went through a new short period of
601 increased activity, with a stronger plume which rotated eastwards during the night of 6-7 June
602 and deposited the lapilli-bearing layer H.
603 Starting on the morning of 7 June, Unit III deposits were emplaced; available activity bulletins
604 (GVP) refer to lower plumes until 15 June (5.5 to 10 km high on 7, between 3.5 and 5.5 km
605 from 7 to 15) which occasionally rose to 7-8 km. This matches well with the deposits, made of
606 ash-bearing beds interlayered with at least two coarser layers (K2 and K4).
607 The correlation among deposits, satellite images and direct accounts of the eruption clearly
608 shows a progressive decrease in intensity of the eruption and the change from sustained, high-
609 level columns typical of subplinian activity to activity dominated by lower magma discharge,
610 diffuse, bent-over plumes and ash emissions. The transition between the two phases occurred
611 during the deposition of Unit II, and ash emissions punctuated by episodes of higher, sustained
612 discharge is recorded in the deposits of Unit III. The large field of ballistic bombs visible in the
613 most proximal areas is clearly associated with this type of activity, and possibly marks the shift
614 to lava effusion (Schipper et al. 2013).

615 Observations of proximal deposits also reveal that up-wind tephra sedimentation was scarce to
616 null, with tephra deposits pinching out hundreds of meters from the vent. This observation
617 suggests that the plume was characterized by a wind-dominated dynamics even during the first,
618 more intense phases of the event (Bonadonna et al. 2015), and that upwind spreading was very
619 limited (stagnation point very close to the plume axis). The bimodality of most grain-size data,
620 even in the more proximal outcrops, also suggests that ash aggregation possibly played an
621 important role during tephra sedimentation (see also Bonadonna et al. submitted).
622

623 ## Insights into eruption dynamics from tephra characteristics

624 Component analyses show a large textural variability in juvenile material throughout the whole
625 deposit. Conversely, both the amount and lithologic variability of lithic material are restricted.
626 The occurrence of lithic material in Unit I and its almost total disappearance thereafter suggest
627 that the major phase of conduit/vent enlargement was mainly restricted to this first, higher
628 discharge phase of the eruption (Bonadonna et al. 2015). Surprisingly, hydrothermally altered
629 rocks form only a very low percentage of lithic fragments, despite the very large geothermal
630 field associated with the Cordón Caulle structure (Sepulveda et al. 2005). This suggests that
631 most of the lithic clasts result from shallow conduit enlargement, rather than from deep
632 conduit erosion, and that this conduit structure did not progressively enlarge during the
633 eruption, in agreement with the general decrease in magma discharge.
634 High-resolution satellite images (Schipper et al. 2013) and sparse direct accounts (GVN) also
635 reveal that, at different times during the eruption, more than one vent was active, possibly
636 aligned along the main structural lineaments of Cordón Caulle (N145; N165). We suggest that
637 the coexistence of many different types of juvenile material within each single tephra layer is
638 consistent with magma ascent through a fissure rather than through a “cylindrical” conduit. The

639 abundance of obsidian could be explained, in this interpretation, by rapid quenching and
640 degassing of magma ascending slowly through the narrower portions of the conduit, while the
641 abundant, highly vesicular, pumice fraction could represent the most rapidly ascending part. In
642 this model, the large abundance of fine-grained clasts of obsidian erupted on 6 June,
643 immediately after the end of the most intense phase of the eruption, could be related to the
644 opening of a new vent along the eruptive fissure.
645 The abundant banded pumice within Unit II and mainly Unit III is lithologically similar to the
646 material forming the glassy ballistic bombs emplaced around the vent by the end of Unit II
647 (layer H) and the start of Unit III (layers K). The coexistence of vesicular and dense, obsidian-like
648 bands testifies to complex interactions between gas-rich and gas-depleted magma portions
649 during ascent to the surface.
650 The composition of the microlite-free, shallow-residing magma feeding the eruption did not
651 change significantly during the event; bulk rock chemistry of juvenile clasts is rather
652 homogeneous throughout the eruption, mostly clustered within the rhyolitic field, with only
653 Unit III pumice showing a slightly more evolved composition. The large variety of juvenile
654 components within the tephra deposits, and the transitions in eruptive dynamics during the
655 eruption, cannot be explained by changes in magma composition and rheology; instead, they
656 possibly relate to a complex magma outgassing history and/or to vertical and lateral variability
657 within the magma column.
658

659 ## Inferences on magma ascent processes from clast vesicularity

660 The observed variations in the relative proportions of juvenile components during the eruption
661 show that heterogeneities increase with the decrease in eruptive intensity. As pointed out by
662 Castro et al. (2013) and Schipper et al. (2013), the efficiency of magma outgassing during ascent

663 may have controlled the intensity of the first explosive phase and the subsequent progression
664 from early pyroclastic venting to later effusive eruption.
665 Schipper et al. (2013) suggested that a highly connected vesicularity had developed after the
666 end of the first, more energetic phase, which they considered as evidence for open-system
667 degassing during this phase of the eruption. This suggestion was based on the presence of
668 tubular, prolate pumice clasts in the tephra during the late stage of the eruption (January
669 2012), when activity was dominated by lava effusion and vulcanian explosions, and on the
670 vesicularity observed in some bombs ejected during a preceding phase. Our careful observation
671 of the juvenile material from the different layers of the first week of the eruption (the phase
672 with the highest mass flow rates; Bonadonna et al. 2015) shows that tubular pumice is present
673 only during phases dominated by ash emission, while the most intense phases that emplaced
674 the main lapilli beds are dominated by subequant, highly vesicular pumice with a highly
675 contorted vesicles.
676 These clasts also present clear evidence of important shear localization (Fig. 15), a factor which
677 largely influences degassing and outgassing and magma ascent rate (Okumura et al. 2009,
678 2013). We suggest that the high magma discharge during the most intense phases resulted in a
679 larger strain rate with respect to the phases of lower intensity (e.g. G, K1, K3, K5), which
680 triggered shear localization in a relatively narrow conduit; shear localization allowed a high flow
681 rate by decreasing the apparent viscosity of the magma (Wright and Weindberg 2009). Another
682 important effect of shear localization is creation bands of highly deformed, elongate, connected
683 vesicles and insulation of large areas of very minor deformation, characterized by nearly
684 spherical, poorly coalescent vesicles. We suggest that this kept bulk magma permeability at a
685 lower level relative to that measured for the tubular vesicularity of the following phases
686 (Schipper et al., 2013). The coexistence of high ascent rate and relatively low permeability of

687 the magma column due to the strongly complex vesicularity stabilized conditions of closed-
688 system degassing. Detailed observations of textures were carried out on the white, vesicular
689 pumiceous fraction only, so that inferences on component variability within the deposits are
690 not straightforward. However, during lower intensity phases (e.g. G or K), higher magma
691 permeability resulted from the development of a continuous, un-interrupted tubular
692 vesicularity. This could possibly favor open-system outgassing resulting in banded or denser
693 clasts characterized by collapsed vesicles, with obsidian clasts the end member of this process.
694

695 ## Comparison with rhyolitic small-moderate eruptions

696 Few studies and observations exist on small-moderate rhyolitic eruptions. Available data
697 suggest that, in general, these events are characterized by complex stratigraphic architectures
698 of tephra deposits mainly due to unsteady column dynamics and PDC activity, dome extrusion
699 or transitions from explosive to effusive phases (e.g. Southern Mono Crater, Bursik et al. 2014;
700 Chaitén, Alfano et al. 2011; Taranaki, Platz et al. 2007). In particular, the progression from mid-
701 intensity explosive activity to a lower intensity, simultaneous explosive-effusive eruption is a
702 characteristic of several eruptive events involving intermediate to evolved magma. This has
703 been, for example, recently observed at Chaitén in 2008 (Castro and Dingwell 2009; Alfano et
704 al. 2011; Wicks et al. 2011).
705 These events share common stratigraphic features, such as complexity of dispersal patterns
706 due to the long duration and, therefore, to the changes in wind direction and velocity.
707 Nonetheless, the characteristics of the juvenile material can be highly variable, ranging from: i)
708 eruptions characterized by homogeneous juvenile material, mainly composed of rhyolitic
709 pumice with variable texture and obsidian clasts (e.g. 2008 eruption of Chaitén, Alfano et al.
710 2012; 1.8 ka activity of Taupo, Houghton et al. 2010) to ii) events in which the juvenile

componentry shows a large variability, ranging from white to dark rhyolitic pumice to brown or black scoriaceous material, and obsidian clasts (post-64 ka activity of Okataina Volcanic Centre, Jurado-Chichay and Walker 2001; 1960 eruption Cordón Caulle, Daga et al. 2012). This textural and morphological heterogeneity in the juvenile fraction is accompanied in only some eruptions by minor variations in composition (Daga et al. 2012, 2014). The similarity of the lithologic variability of the juvenile fraction described for the 2011 Cordón Caulle eruption (this work and Daga et al. 2014) with the material described for the 1960 event (Daga et al. 2012) is striking. We suggest that at least part of this variability can be related to the clear presence of dyke-like conduits in both the 1960 and 2011 eruptions (Castro et al. 2013), mainly related to the structural setting of the Cordón Caulle complex. This clearly suggests that the large heterogeneity of juvenile types in these events reflects complex dynamics during magma ascent and fragmentation due to wall effects (a low ratio of conduit diameter to conduit walls, along which shear effects are higher) and also complex feeding systems which may undergo variable evolution trends or reactivation cycles.

Conclusions

Our detailed stratigraphic study of the 2011 Cordón Caulle eruption illustrates the following points:

1) Four main eruptive phases are recognized: i) a first phase (4-5 June) with the highest intensity, during which tephra was dispersed towards the east-southeast (Unit I), with a total volume of ca. 0.75 km^3; ii) a second phase (5-6 June) marked by an abrupt wind shift towards the north and possibly after a shift of the vent, leading to the deposition of an obsidian-rich ash deposit (layer G) in the northern sector and by the return to a west wind that dispersed ash eastwards (emplacement of layer H, total volume ca. 0.21 km^3); iii) a third phase (from the

735 morning of 7 June) during which tephra deposits accumulated in the eastern sector (Unit III).
736 This phase was characterized by ballistic bomb emplacement around the vent area,
737 corresponding in mid-distal areas to the coarsest layer (K2, total volume ca. 0.05 km^3); iv) a
738 fourth phase (possibly after 15 June) characterized by the emission of fine-grained white ash
739 from plumes during low-level activity (Unit IV).
740 2) A wide range of juvenile components, with abundant vesicular, white pumice clasts and
741 minor banded and dense juvenile fragments characterize the erupted tephra. The white
742 juvenile fraction has a narrow compositional range, mostly clustering within the rhyolitic field,
743 and is characterized by negligible density variations throughout the eruptive sequence, with a
744 slight increase for layer K2. The large variety of tephra clasts and textural features of the white
745 pumice components suggest possible heterogeneities within the magma column, within which
746 variable strain rate due to variable magma ascent velocity induced strain localization within the
747 clasts and rapid changes in magma degassing efficiency.
748 3) The dynamics of the eruption can be related to the rapid ascent of magma from a
749 homogeneous rhyolitic reservoir, generating a first phase with high plumes and rapid rise rate
750 (i.e. high mass discharge) during which lapilli were emplaced with an increasing lithic content
751 related to vent/conduit enlargement. Due to the high strain rate during magma ascent,
752 vesicular material of this phase is characterized by evident strain localization disturbing
753 vesicularity and decreasing average bubble connectivity. During the following phases, lower
754 mass discharge (resulting in lower strain rate) possibly favored open-system degassing, and
755 juvenile clasts do not show evidence of shear localization. The decreasing intensity of the
756 eruption finally led to extrusion of lava and to a shift towards vulcanian activity characterized
757 by emplacement of ash deposits and ballistic bombs.

4) Regardless of the short duration of the initial, intense phases of the event, stratigraphic reconstruction reveals a complex tephra stratigraphy related to wind shifts and oscillations in eruptive intensity. Detailed study of this mid-intensity eruption clearly illustrates the complex time evolution (changes in eruptive style and eruptive regime) characteristic of these types of events, and highlights the need for very detailed field surveys of the deposits of such eruptions in order to fully capture their dynamics.

Acknowledgments

M. Pistolesi, R. Cioni, A. Bertagnini and L. Francalanci were supported by Italian Ministero Universita' e Ricerca funds (PRIN 2008 – AshErupt project, managed by R. Cioni). C. Bonadonna was supported by Swiss National Science Foundation (SNSF; No 200020_125024). Authors are grateful to L. Dominguez for the laser grain-size analyses and to P. Sruoga for her assistance in the field. D.A. Swanson and the Associate Editor V. Manville are acknowledged for their constructive comments on the manuscripts.

References

Adams NK, Houghton BF, Fagents SA, Hildreth W (2013) The transition from explosive to effusive eruptive regime: The example of the 1912 Novarupta eruption, Alaska. Geol Soc Am Bull 118(5-6):620–634. doi:10.1130/B25768.1

Alfano F, Bonadonna C, Volentik ACM, Connor CB, Watt SFL, Pyle DM, Connor LJ (2011) Tephra stratigraphy and eruptive volume of the May, 2008, Chaitén eruption, Chile. Bull Volcanol 73:613–630

Alfano F, Bonadonna C, and Gurioli L (2012) Insights into eruption dynamics from textural analysis: the case of the May, 2008, Chaitén eruption. Bull Volc doi: 10.1007/s00445-012-0648-3.

Bonadonna C, and Houghton BF (2005) Total grain-size distribution and volume of tephra- fall deposits. Bull Volcanol 67:441–456. doi:10.1007/s00445-004-0386-2

Bonadonna C, and Costa A (2012) Estimating the volume of tephra deposits: A new simple strategy. Geology 40:415-418. doi: 10.1130/G32769.1

Bonadonna C, Pistolesi M, Cioni R, Degruyter W, Elissondo M, Baumann V (2015). Dynamics of wind-affected volcanic plumes: the example of the 2011 Cordón Caulle eruption, Chile. J Geophys Res-Solid Earth, in press.

Bonadonna C, Cioni R, Pistolesi M, Elissondo M, Baumann V (submitted). Sedimentation of long-lasting wind-affected volcanic plumes: the example of the 2011 rhyolitic Cordón Caulle eruption, Chile. Bull Volc

Bursik M (1993) Subplinian eruption mechanisms inferred from volatile and clast dispersal data. J Volcanol Geotherm Res 57:57–70

795 Bursik M, Sieh K, and Meltzner A (2014) Deposits of the most recent eruption in the Southern
796 Mono Craters, California: Description, interpretation and implications for regional marker
797 tephras. J Volc Geoth Res 275:114–131, doi: 10.1016/j.jvolgeores.2014.02.015
798 Cashman K, Blundy J (2000) Degassing and crystallization of ascending andesite. Royal Soc Lond
799 Philos Trans 358:1487–1513
800 Castro JM, Dingwell DB (2009) Rapid ascent of rhyolite magma at Chaitén volcano, Chile. Nature
801 461:780–784
802 Castro JM, Schipper CI, Mueller SP, Militzer AS, Amigo A, Parejas CS, Jacob D (2013) Storage and
803 eruption of near-liquidus rhyolite magma at Cordón Caulle, Chile. Bull Volcanol 75, 702
804 Cioni R, Marianelli P, Santacroce R, Sbrana A (2000) Plinian and subplinian eruptions. In:
805 Sigurdsson H, Houghton B, McNutt SR, Rymer H, Stix J (eds) Encyclopedia of volcanoes.
806 Academic, San Diego, pp 477–494
807 Collini E, Osores MS, Folch A, Viramonte JG, Villarosa G, Salmuni G (2012) Volcanic ash forecast
808 during the June 2011 Cordón Caulle eruption. Nat Haz 66:389-412
809 Daga R, Castro A, La Rosa DJ, Ribeiro Guevara S, Sánchez ML, and Arribére M (2012)
810 Heterogeneidades texturales y composicionales en productos piroclásticos de la erupción
811 de 1960 del sistema Cordón Caulle (40° 30“S, 72° 10”O). Rev Asoc Geol Arg 69(4):496–507
812 Daga R, Guevara SR, Poire DG, and Arribére M (2014) Characterization of tephras dispersed by
813 the recent eruptions of volcanoes Calbuco (1961), ChaitEn (2008) and Cordón Caulle
814 Complex (1960 and 2011), in Northern Patagonia. J South Am Earth Sci 49:1–14, doi:
815 10.1016/j.jsames.2013.10.006
816 Eychenne J, Le Pennec JL (2012) Sigmoidal particle density distribution in a subplinian scoria fall
817 deposit. Bull Volcanol 74:2243–2249 DOI 10.1007/s00445-012-0671-4
818 Folk RL, Ward WC (1957) Brazos river bar: a study in the significance of grain-size parameters. J
819 Sed Petrol 27:3–26
820 Genareau K, Valentine GA, Moore G, Hervig RL (2010) Mechanisms for transition in eruptive
821 style at a monogenetic scoria cone revealed by microtextural analyses (Lathrop Wells
822 volcano, Nevada, U.S.A.). Bull Volcanol 72:593–607. doi: 10.1007/s00445-010-0345-z
823 Houghton BF, Wilson CJN (1989) A vesicularity index for pyroclastic deposits, Bull Volcanol
824 51:451–462
825 Houghton BF, Gonnerman HM (2008) Basaltic explosive volcanism: constraints from deposits
826 and models. Chemie der Erde Geo-chemistry 68:117–140
827 Houghton BF, Carey RJ, Cashman KV, Wilson CJN, Hobden BJ, Hammer JE (2010) Diverse
828 patterns of ascent, degassing, and eruption of rhyolite magma during the 1.8ka Taupo
829 eruption, New Zealand: Evidence from clast vesicularity. J Volc Geoth Res 195(1), 31–47,
830 doi:10.1016/j.jvolgeores.2010.06.002
831 Kanamori H, Cipar JJ (1974) Focal process of the great Chilean earthquake, May 22, 1960. Phys.
832 Earth Planet. Inter. 9:128–136
833 Katsui J, Katz H. (1967) Lateral fissure eruptions in the Southern Andes of Chile. Fac. Sci. Ser. 4,
834 433–448 (Hokkaido)
835 Inman DL (1952) Measures for describing the size distribution of sediments: J Sed Pet 22:125–
836 145
837 Jay, J., Costa, F., Pritchard, M., Lara, L., Singer, B., and Herrin, J. (2014) Locating magma
838 reservoirs using InSAR and petrology before and during the 2011–2012 Cordón Caulle silicic
839 eruption: Earth Planet Sci Lett 395:254–266
840 Jurado-Chichay Z, and Walker GPL (2001) Variability of plinian fall deposits: examples from
841 Okataina Volcanic Centre, New Zealand. J Volcanol Geotherm Res 111(1), 239–263

842 Lara LE, Naranjo JA, Moreno H. (2004) Rhyodacitic fissure eruption in Southern Andes (Cordón
843 Caulle; 40.5°S) after the 1960 (Mw:9.5) Chilean earthquake: a structural interpretation. J
844 Volcanol Geotherm Res 138:127–138
845 Lara LE, Moreno H, Naranjo JA, Matthews S, Pérez de Arce C (2006) Magmatic evolution of the
846 Puyehue–Cordón Caulle Volcanic Complex (40° S), Southern Andean Volcanic Zone: From
847 shield to unusual rhyolitic fissure volcanism. J Volcanol Geotherm Res 157:343–366
848 Le Bas MJ, Le Maitre RW, Streckeisen A, and Zanettin B. (1986) A chemical classification of
849 volcanic rocks based on the total alkali-silica diagram. Journal of Petrology, 27, 745-750
850 Lowell TV, Heusser CJ, Andersen BG, Moreno PI, Hauser A, Heusser LE, Schluchter C, Marchant
851 DR, Denton GH (1995) Interhemispheric correlation of late Pleistocene glacial events.
852 Science 269:1541–1549
853 Masciocchi M, Pereira AJ, Lantschner MV, Corley JC (2013) Of volcanoes and insects: the impact
854 of the Puyehue–Cordón Caulle ash fall on populations of invasive social wasps, Vespula spp.
855 Ecol Res 28(2):199-205
856 Moreno H, Petit-Breuilh ME, (1999) El volcán fisural Cordón Caulle, Andes del Sur (40.5°S):
857 geología general y comportamiento eruptivo histórico. 14th Congreso Geológico Argentino,
858 Actas 2:258–260. Salta
859 Morrissey MM, Mastin LG (2000) Vulcanian eruptions. In: Sigurdsson H, Houghton B, McNutt
860 SR, Rymer H, Stix J (eds) Encyclopedia of volcanoes. Academic, San Diego, pp 463–475
861 Okumura S, Nakamura M, Takeuchi S, Tsuchiyama A, Nakano T, Uesugi K. (2009) Magma
862 deformation may induce non-explosive volcanism via degassing through bubble networks.
863 Earth Planet Sci Lett 281:267–274
864 Okumura S, Nakamura M, Uesugi K, Nakano T, Fujioka T (2013) Coupled effect of magma
865 degassing and rheology on silicic volcanism. Earth Planet Sci Lett 362:163–170
866 Platz T, Cronin SJ, Cashman KV, Stewart RB and Smith IEM (2007) Transition from effusive to
867 explosive phases in andesite eruptions — A case-study from the AD1655 eruption of Mt.
868 Taranaki, New Zealand. J Volc Geoth Res 161(1-2):15–34.
869 doi:10.1016/j.jvolgeores.2006.11.005
870 Pyle DM (1989) The thickness, volume and grain-size of tephra fall deposits. Bull Volcanol 51:1–
871 15. doi:10.1007/BF01086757.
872 Schipper CI, Castro JM, Tuffen H, James MR, How P (2013) Shallow vent architecture during
873 hybrid explosive-effusive activity at Cordón Caulle (Chile, 2011-12): Evidence from direct
874 observations and pyroclast textures. J Volc Geoth Res 262:25-37.
875 doi:10.1016/j.jvolgeores.2013.06.005
876 Sepúlveda F, Lahsen A, Bonavalot S, Cembrano J, Alvarado A, and Letelier P. (2005) Morpho-
877 structural evolution of the Cordón-Caulle geothermal region, Southern Volcanic Zone,
878 Chile: Insights from gravity and 40Ar/39Ar dating. J Volc Geoth Res 48:165–189
879 Silva Parejas C, Lara LE, Bertin D, Amigo A, Orozco G (2012) The 2011–2012 eruption of Cordón
880 Caulle volcano (Southern Andes): evolution, crisis management and current hazards. EGU
881 General Assembly 2012, Vienna, Austria, 22–27 April 2012. p. 9382
882 Simkin T, Siebert L (2000) Earth's volcanoes and eruptions: An overview. In: Sigurdsson H,
883 Houghton BF, McNutt SR, Rymer H, Stix J (Eds.), Encyclopedia of Volcanoes. Academic
884 Press, San Diego, 249–269
885 Singer BS, Jicha BR, Harper MA, Naranjo JA, Lara LE, Moreno-Roa H (2011) Eruptive history,
886 geochronology, and magmatic evolution of the Puyehue-Cordón Caulle volcanic complex,
887 Chile. Geol Soc Am Bull 120:599–618
888 Tuffen H, James MR, Castro JM, Schipper CI (2013) Exceptional mobility of an advancing

rhyolitic obsidian flow at Cordón Caulle volcano in Chile. Nat Commun 4:2709 doi:10.1038/ncomms3709
Villemant B, Boudon G (1998) Transition from dome-forming to plinian eruptive styles controlled by H_2O and Cl degassing. Nature 392(6671):65–69
Wicks C, de la Llera JC, Lara LE, Lowenstern J (2011) The role of dyking and fault control in the rapid onset of eruption at Chaitén volcano, Chile. Nature 478:374–377
Wong LJ, Larsen JF (2010) The Middle Scoria sequence: a Holocene violent strombolian, subplinian and phreatomagmatic eruption of Okmok volcano, Alaska. Bull Volcanol 72:17–31
Wright HMN and Weinberg RF (2009) Strain localization in vesicular magma: Implications for rheology and fragmentation. Geology 37:1023–1026

Figure captions

Figure 1

(A) Shaded relief map of the Puyehue-Cordón Caulle area. Surveyed outcrops are indicated (different colors and symbols denote different field campaigns). Black and white stars indicate Puyehue volcano and the 2011 vent, respectively. Locations and numbers of the key sections used in the text are also indicated. The black square represents the enlarged area in (B). In (B), the black line shows the Chile-Argentina border, the red lines refer to the intersection between the Liquiñe-Ofqui Fault and the Cordón Caulle graben.

Figure 2

(A) Locations of the pictures used in Figs. 2 and 3. (B) The tephra sequence on July 2011 at section 3 (Paso Cardenal Samoré, 28 km from the vent). (C) Layers F, H, and K at section 4 (Lago Espejo, 42 km from the vent). (D) The tephra sequence 100 km east of the vent.

Figure 3

(A) Layers A to F become difficult to separate within the sequence 5 km west of section 3, along the route towards the Chile-Argentina border. (B) The tephra sequence at section 5 (in the town of Villa La Angostura, 48 km from the vent). (C) Snow intercalations in the tephra

sequence observed in July 2011, 40 km east from the vent. (D) The tephra sequence on a tomb stone at section 7 (Ingeniero Jacobacci, 240 km east of the vent).

Figure 4

Stratigraphic correlations among different outcrops. A-A' includes key sections along the main dispersal axis. B-B' and C-C' are transects across the main dispersal axis.

Figure 5

(A) The 2011 lava flow front and the vent area seen from the west; the tephra cone and the Puyehue volcano are visible in the background. (B) The tephra sequence 1 km upwind from the vent. (C) Black obsidian bomb in proximal area. (D) Scoriaceous, banded bombs in the vent area. (E) Welded breccia in inner part of a bomb.

Figure 6

(A) Close-up aerial view of the vent area; note the portions of the tephra cone engulfed by the active lava flow. Black and white boxes refer to images in (D) and (B), respectively. (B) Impact crater area north of the active vent. Inset shows variation of the impact crater density (number/km^2) with distance from vent. (C) Inferred area of PDC deposits from satellite images. (D) Detailed view of the fallen trees in different directions due to the passage of multiple PDCs.

Figure 7

NOAA-GOES satellite images taken during the eruption (5, 6, 7 and 8 June 2011) at ca. 16:00 local time (LCT). The vent area is indicated with the red circle and the plumes are highlighted in red.

Figure 8

(A) Isopach maps in cm of layers A-B, A-F, H and K2. The inferred limit of the deposits (dashed lines) is also indicated.

941 Figure 9

942 Plots of log thickness versus square root of area for four fallout tephra layers (A-B, A-F, H and
943 K2), showing exponential (black lines), power-law (yellow curves) and Weibull (red curves) best
944 fits. Diamonds represent field data.

945 Figure 10

946 Stratigraphic section of the tephra sequence at Río Gol Gol, 15 km SE of the vent area (section
947 2). Grain-size distributions, Mdϕ, $\sigma\phi$, componentry and chemical variations (Sr and Th) for the
948 main tephra layers are shown. Width of stratigraphic column scales with grain-size. Variation
949 bars for Sr and Th refer to the standard deviations of analyses made on different selected
950 clasts.

951 Figure 11

952 Stratigraphic section of the tephra sequence at Paso Cardenal Samoré, 28 km SE of the vent
953 area (section 3). Grain-size distributions, Mdϕ, $\sigma\phi$ and componentry variations for the main
954 tephra layers are shown. Width of stratigraphic column scales with grain-size.

955 Figure 12

956 Stratigraphic sections of the tephra sequence at the vent area, Villa La Angostura and Ingeniero
957 Jacobacci (sections 1, 5 and 7, respectively). Grain-size and sorting variations for the main
958 tephra layers are shown, as are componentry analyses for layer G (section 1) and for the
959 sequence at section 5. Width of stratigraphic column scales with grain-size.

960 Figure 13

961 Images of juvenile (A) white pumice, (B) banded pumice, (C) dense and (D) obsidian clasts.
962 Macroscopic images of clasts on the left, SEM backscattered images in the center and plane-
963 polarized light thin section pictures on the right.

964 Figure 14

965 (A) Vesicularity and density distributions for juvenile vesicular fragments collected from layers
966 B, D, F, H and K2. (B) Plots of mean particle densities (in kg/m^3) in the grain-size fractions (-4 to
967 1ϕ) for layers C, F and K2 collected at section 4. Symbol size is larger than the error bar defined
968 as ±1 standard deviation (1σ; evaluated from the results of three sets of measurements
969 performed on a sample for each size class). Red star refer to the measured DRE values.

970 Figure 15

971 SEM back-scattered images of vesicular fragments from layer H (A), layer C (B, C, D, F), layer A
972 (E), and layer G (G, H). White lines and arrows refer to areas with contrasting vesicularity and
973 shear localization.

974

975 Table 1

976 Grain-size and componentry data of representative samples collected at the key sections.
977 Modes 1 and 2 are indicated for bimodal samples. Mdϕ and $\sigma\phi$ are the median and the
978 standard deviation of the size distribution, respectively, with ϕ=-log$_2$D (where D is the particle
979 diameter in millimeters). F1 and F2 represent the weight sample fraction <1 mm and <63 μm,
980 respectively.

981 Table 2

982 Satellite image sources and average plume directions from 4 to 9 June 2011 for the different
983 layers.

984 Table 3

985 Volumes (km^3) calculated using different strategies (see main text for details). Average and
986 standard deviation based on all strategies are shown in the last column (considering only the 3

exponential segments for A-F). Uncertainty for the power-law calculation is derived based on different distal extreme of integrations (200, 500 and 700 km for A-B; 700, 1000 and 1500 km from vent for A-F, H and K2). Given that the power-law exponent is >2 for all layers, the volume is mostly sensitive to the proximal integration limit, which was calculated based on the eq. 7 of Bonadonna and Houghton (2005) for all layers.

Table ESM1

Thickness data for each stratigraphic layer measured at each location. Numbers of outcrops and geographic coordinates (UTM, WGS 1984-Zone 19 South) are also reported. Key sections described in the text are indicated in brackets.

Table ESM2

Whole-rock major and trace element analyses. Values are averages of 2-3 analyses for each layer made on different selected clasts. Key sections 3 and 4 correspond to section 001 (Cardenal Samorè) and 004 (Lago Espejo), respectively.

Table 1

Layer	Unit	Dist. (km)	Section	MdΦ	σΦ	Sorting	F1	F2	Mode 1	Mode 2	White pum.	Banded pum.	Dense juven.	Obsidians	Crystals	Lithics (tot.)
A	I	15	2 - Gol Gol	-3.10	1.54	Well sorted	4.40	2.25	-3.7	4.6	88.3	0.4	1.6	0.2	1.0	8.6
B	I	15	2 - Gol Gol	-2.79	1.58	Well sorted	3.84	1.91	-3.6	4.9	72.4	3.6	0.9	0.2	0.6	22.3
C	I	15	2 - Gol Gol	-2.89	1.56	Well sorted	3.57	1.64	-3.06	4.83	71.1	2.5	0.4	0.1	0.7	25.2
D	I	15	2 - Gol Gol	-2.96	1.50	Well sorted	4.34	2.15	-3.2	4.41	89.6	0.4	0.1	0.3	0.1	9.6
E	I	15	2 - Gol Gol	-2.68	1.72	Well sorted	5.19	2.21	-2.84	4.85	85.1	1.4	1.2	0.6	0.1	11.6
F	I	15	2 - Gol Gol	-3.11	1.68	Well sorted	5.28	1.68	-3.35	4.88	82.0	7.9	0.1	4.4	0	5.6
H	II	15	2 - Gol Gol	-0.82	1.57	Well sorted	16.51	5.79	-0.95	5.19	89.5	5.9	0.8	1.7	1.0	1.1
K2	III	15	2 - Gol Gol	-1.62	1.25	Well sorted	11.30	7.80	-1.76	5.17	88.0	8.1	0.2	1.4	1.8	0.5
K4	III	15	2 - Gol Gol	-0.57	1.43	Well sorted	22.52	9.39	-0.73	4.78	95.5	2.5	0.1	0.1	0	0.4
AF	I	15	2 - Gol Gol	-2.34	1.80	Well sorted	5.48	2.45	-2.47	5.08	–	–	–	–	–	–
G		1	1 - Vent	0.32	2.99	Poorly sorted	44.36	18.82	0.06	5.76	59.0	11.2	1.2	27.6	0	1.0
A	I	28	3 - Samoré	-2.46	1.16	Well sorted	2.11	1.75	-2.52	5.88	86.9	0.1	2.6	0.2	1.2	9.1
B	I	28	3 - Samoré	-3.20	1.29	Well sorted	5.38	2.81	-3.46	5.81	92.8	0.3	0.6	0.03	0.7	5.6
C	I	28	3 - Samoré	-2.22	1.33	Well sorted	4.66	2.41	-2.3	5.95	77.8	1.5	1	0.2	1	18,5
D	I	28	3 - Samoré	-2.64	1.56	Well sorted	7.03	3.26	-2.86	5.5	85.7	0.8	1	0.2	0.9	11.6
E	I	28	3 - Samoré	-1.86	1.53	Well sorted	8.16	2.52	-1.98	5.93	78.9	3.2	1.6	0.4	1	14.9
F	I	28	3 - Samoré	-1.80	1.51	Well sorted	11.06	5.29	-1.98	5.51	72.7	3.3	3.6	0.4	1	19
AF	I	28	3 - Samoré	-2.45	1.48	Well sorted	4.44	1.48	-2.58	5.55	–	–	–	–	–	–
K1	III	28	3 - Samoré	0.39	3.36	Poorly sorted	47.28	31.33	-0.22	5.76	90.8	7.6	0	0.4	0.8	0.4
K2	III	28	3 - Samoré	1.74	3.19	Poorly sorted	63.55	27.99	-0.11	4.72	93.2	5.6	0	0.3	0.6	0.4
AF	I	42	4 - Espejo	-0.12	1.14	Well sorted	29.53	1.53	-0.09	6.13	–	–	–	–	–	–
H	II	42	4 - Espejo	0.77	0.34	Very well sort.	83.92	4.59	0.77	6.42	–	–	–	–	–	–
K1	III	42	4 - Espejo	0.88	2.07	Poorly sorted	54.26	2.81	0.78	5.64	–	–	–	–	–	–
K2	III	42	4 - Espejo	-0.18	3.16	Poorly sorted	96.44	26.45	-0.56	5.56	–	–	–	–	–	–
K3	III	42	4 - Espejo	4.47	2.68	Poorly sorted	30.9	21.02	1.3	5.05	–	–	–	–	–	–
AF	I	48	5-V. La Ang.	-0.20	1.21	Well sorted	25.59	4.37	-0.32	3.11	89.9	7.0	0.8	0.5	0.4	1.3
H base	II	48	5-V. La Ang.	0.55	0.61	Very well sort.	63.55	27.99	0.58	6.54	–	–	–	–	–	–
H top	II	48	5-V. La Ang.	0.99	0.65	Very well sort.	31.39	1.62	0.9	4.8	97.7	1.7	0	0.4	0.1	0.1
K1	III	48	5-V. La Ang.	4.20	2.83	Poorly sorted	93.34	46.06	0.9	5.18	–	–	–	–	–	–
K2	III	48	5-V. La Ang.	0.40	3.33	Poorly sorted	47.83	30.46	-0.44	5.13	93.2	4.8	0	0.4	1.3	0.3
K3-5	III	48	5-V. La Ang.	4.11	2.50	Poorly sorted	97.44	44.61	1.57	5.15	–	–	–	–	–	–
AF	I	240	7 - Jacobacci	5.36	1.53	Well sorted	100	74.88	–	5.41	–	–	–	–	–	–
K1	III	240	7 - Jacobacci	5.34	1.50	Well sorted	100	75.52	–	5.34	–	–	–	–	–	–
K2	III	240	7 - Jacobacci	5.50	1.56	Well sorted	100	77.24	–	5.5	–	–	–	–	–	–
K3	III	240	7 - Jacobacci	5.44	1.56	Well sorted	100	76.49	–	5.44	–	–	–	–	–	–
K4	III	240	7 - Jacobacci	5.37	1.53	Well sorted	100	74.88	–	5.37	–	–	–	–	–	–

Table 2

Date	Time (LTC)	Image source	Av. plume dispersal (deg. from N)	Layer (Unit)
4 June	18:28	GOES	135° (SE)	AF (I)
4 June	18:45	GOES	125° (SE)	AF (I)
4 June	18:50	AQUA	120° (SE)	AF (I)
4 June	19:28	GOES	120° (SE)	AF (I)
4 June	19:45	GOES	120° (SE)	AF (I)
4 June	19:58	GOES	120° (SE)	AF (I)
4 June	20:15	GOES	118° (SE)	AF (I)
5 June	12:28	GOES	123° (SE)	AF (I)
5 June	13:45	TERRA	119° (SE)	AF (I)
5 June	14:45	GOES	118° (SE)	AF (I)
5 June	17:55	AQUA	118° (SE)	AF (I)
5 June	19:45	GOES	115° (SE)	AF (I)
6 June	12:45	GOES	30° (NE) – 126° (SE)	G (II)
6 June	14:25	TERRA	26° (NE) – 125° (SE)	G (II)
6 June	16:45	GOES	25° (NE) – 133° (SE)	G (II)
6 June	18:40	AQUA	25° (NE) – 138° (SE)	G (II)
6 June	19:45	GOES	25° (NE) – 142° (SE)	G (II)
7 June	13:28	GOES	120° (SE)	K2 (III)
7 June	15:10	TERRA	115° (SE)	K2 (III)
7 June	17:45	GOES	110° (SE)	K2 (III)
7 June	19:20	AQUA	110° (SE)	K2 (III)
7 June	19:45	GOES	110° (SE)	K2 (III)
8 June	12:58	GOES	55° (NE)	K3 (III)
8 June	14:15	TERRA	70° (NE)	K3 (III)
8 June	16:28	GOES	50° (NE)	K3 (III)
8 June	18:25	AQUA	50° (NE)	K3 (III)
8 June	19:28	GOES	50° (NE)	K3 (III)
9 June	13:28	GOES	40° (NE)	K4 (III)
9 June	14:55	TERRA	55° (NE)	K4 (III)
9 June	16:28	GOES	50° (NE)	K4 (III)
9 June	17:15	GOES	50° (NE)	K4 (III)
9 June	18:15	GOES	50° (NE)	K4 (III)

Table 3

Layer	Exponential			Power Law	Weibull	Average
	1 segment	2 segments	3 segments			
AB	0.21			0.20 ± 0.00	0.22	0.21± 0.01
AF		0.44	0.56	0.81 ± 0.03	0.88	0.75± 0.17
H		0.13		0.23 ± 0.04	0.27	0.21± 0.07
K2	0.04			0.06 ± 0.00	0.04	0.05± 0.01

Figure 1
Click here to download high resolution image

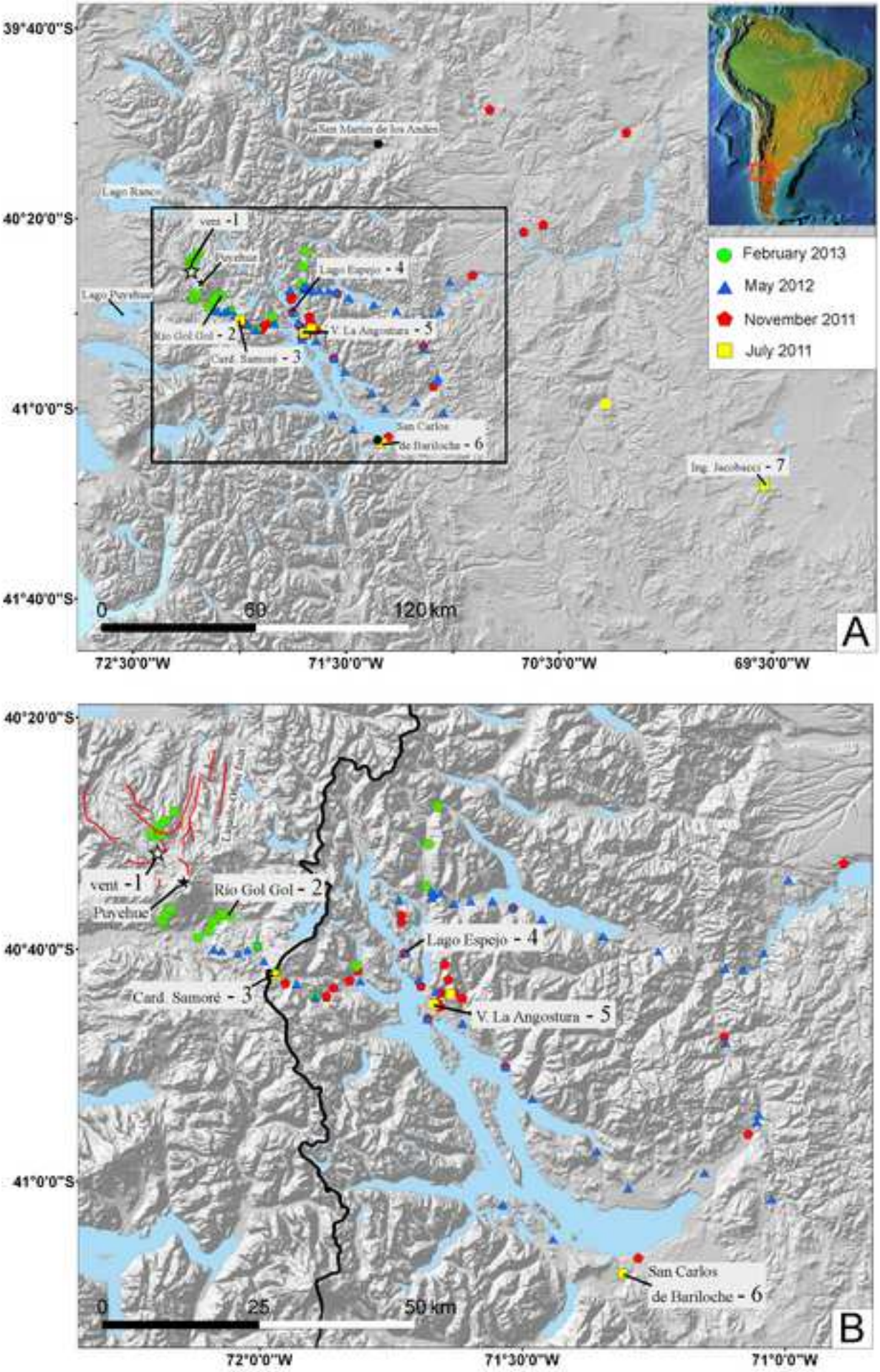

Figure 2
Click here to download high resolution image

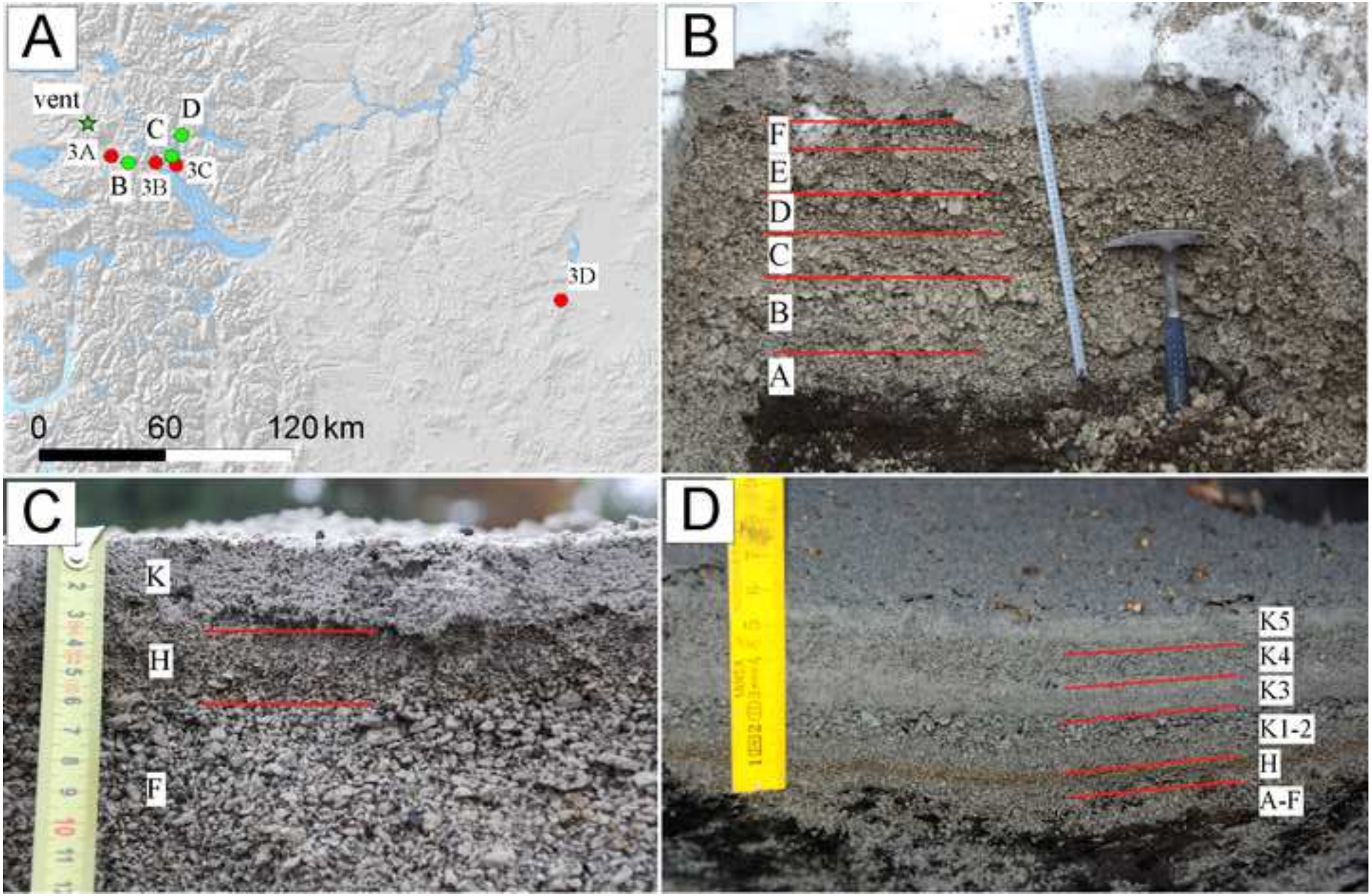

Figure 3
Click here to download high resolution image

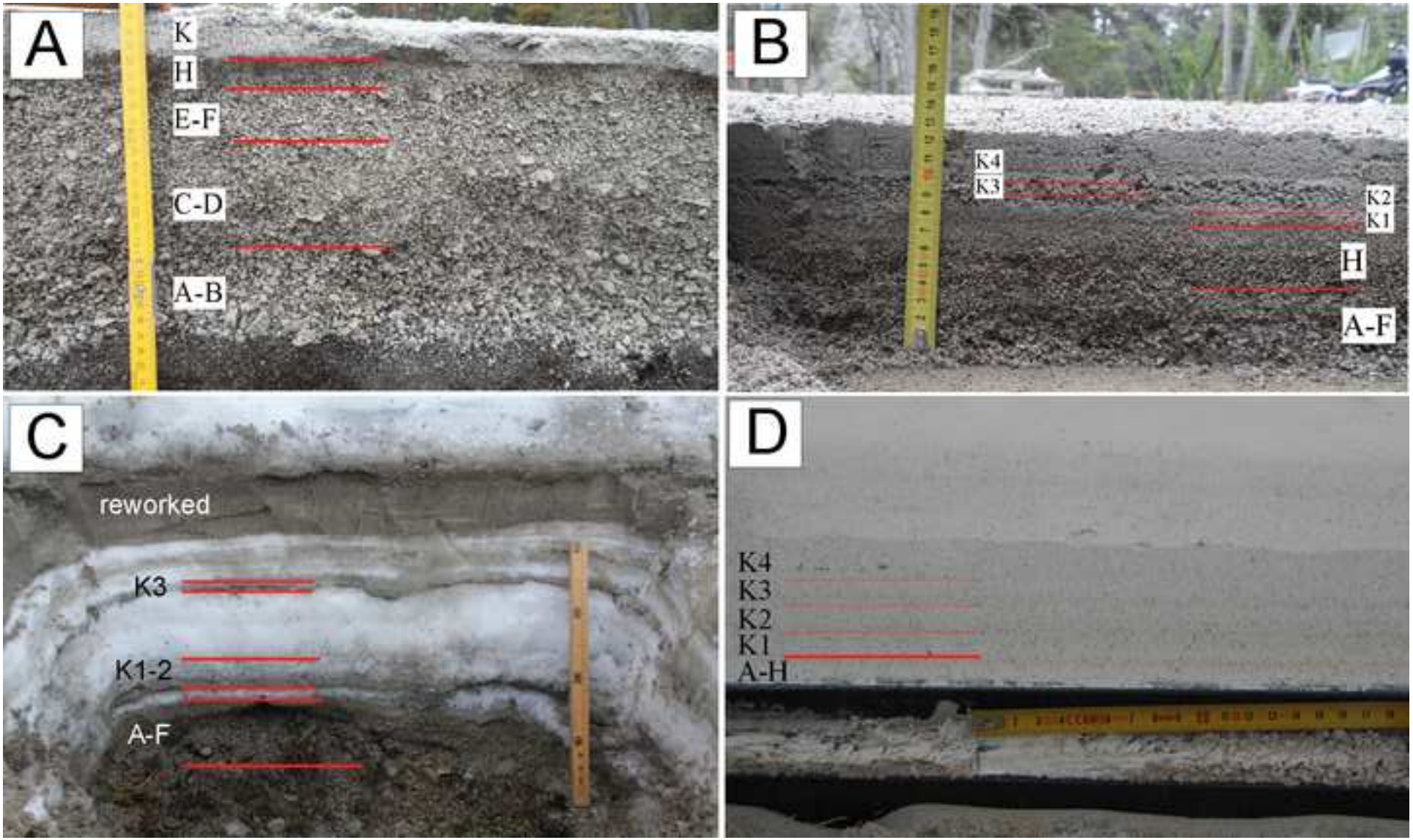

Figure 4

Click here to download high resolution image

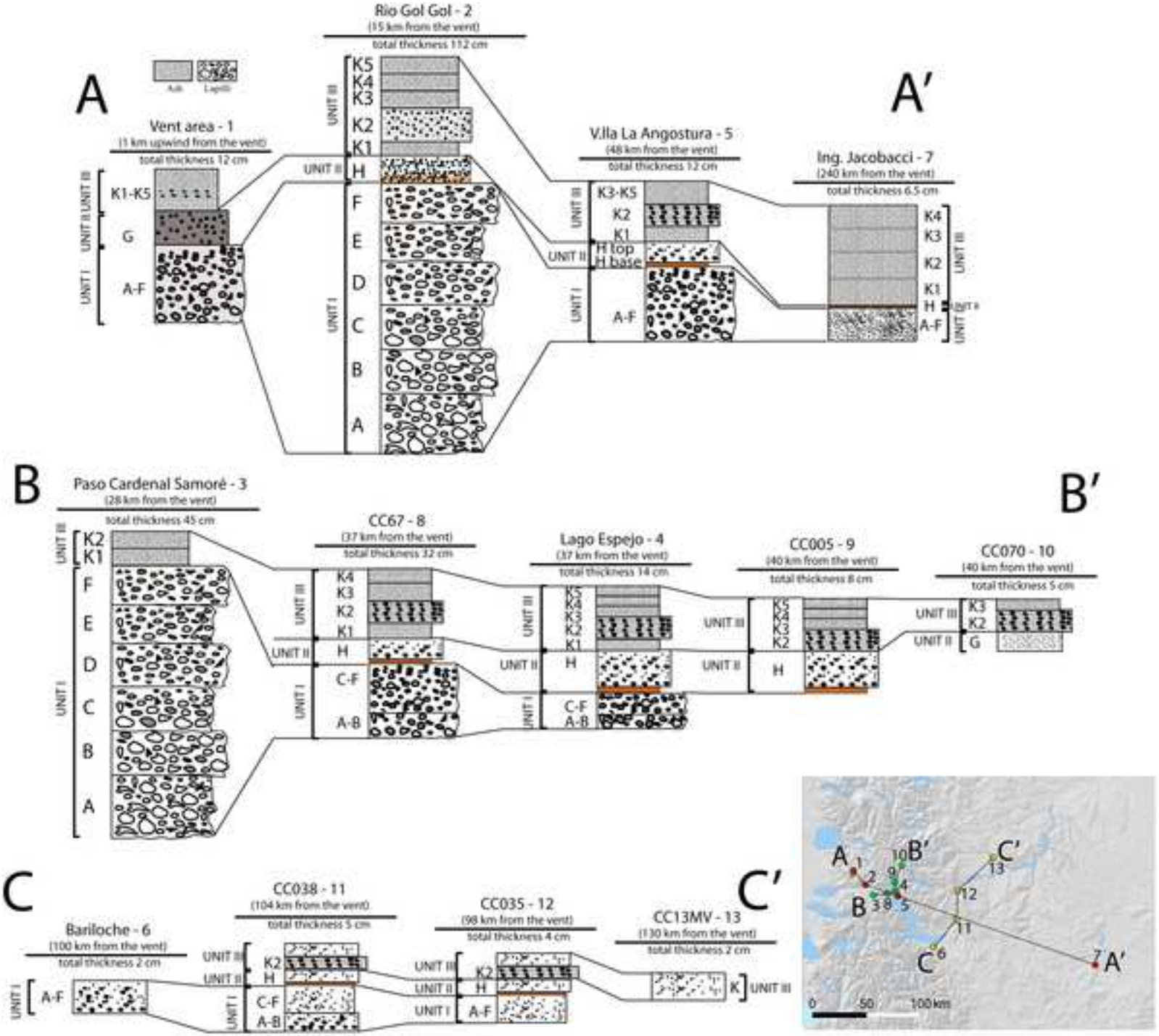

Figure 5
Click here to download high resolution image

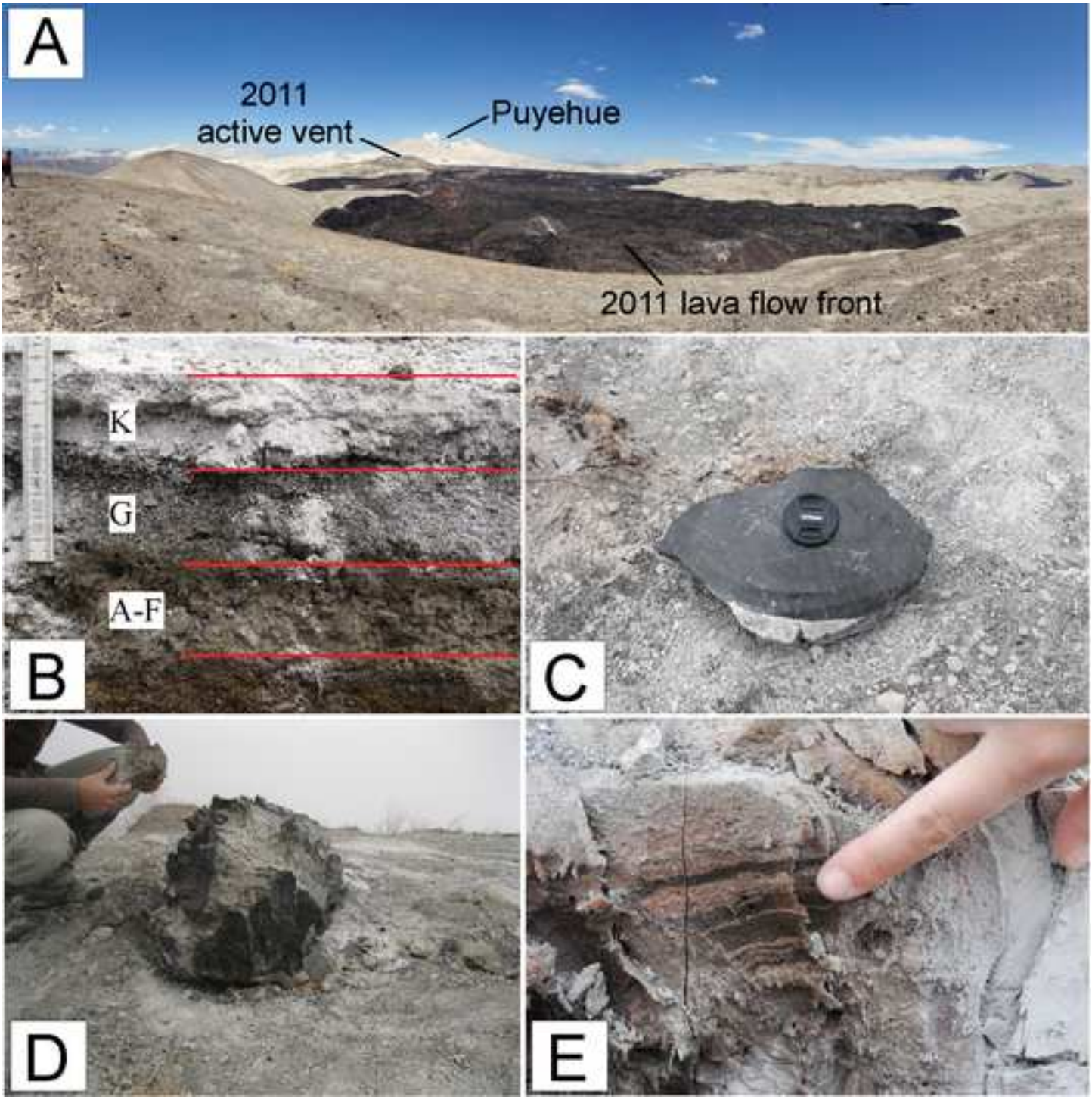

Figure 6
Click here to download high resolution image

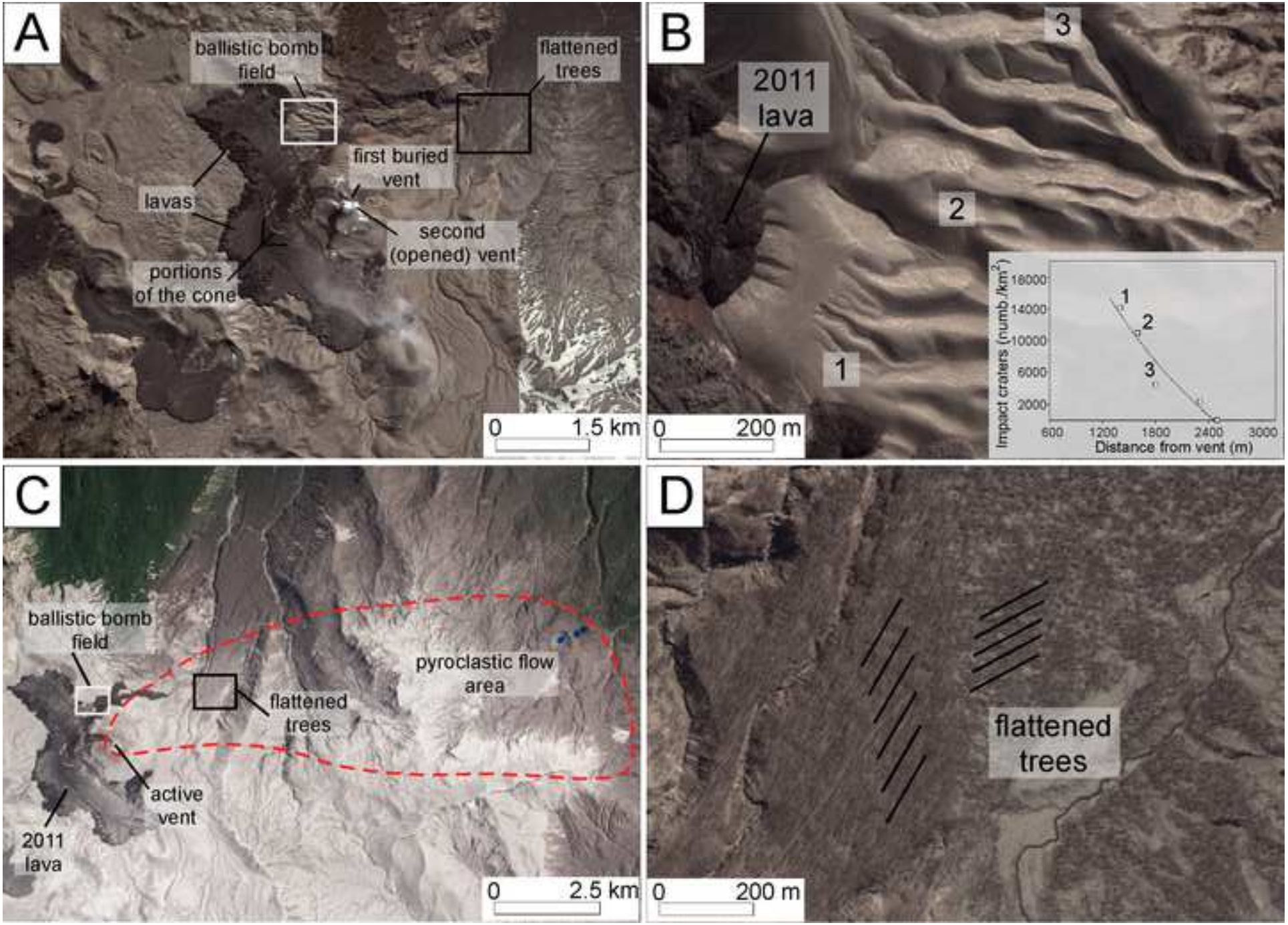

Figure 7
Click here to download high resolution image

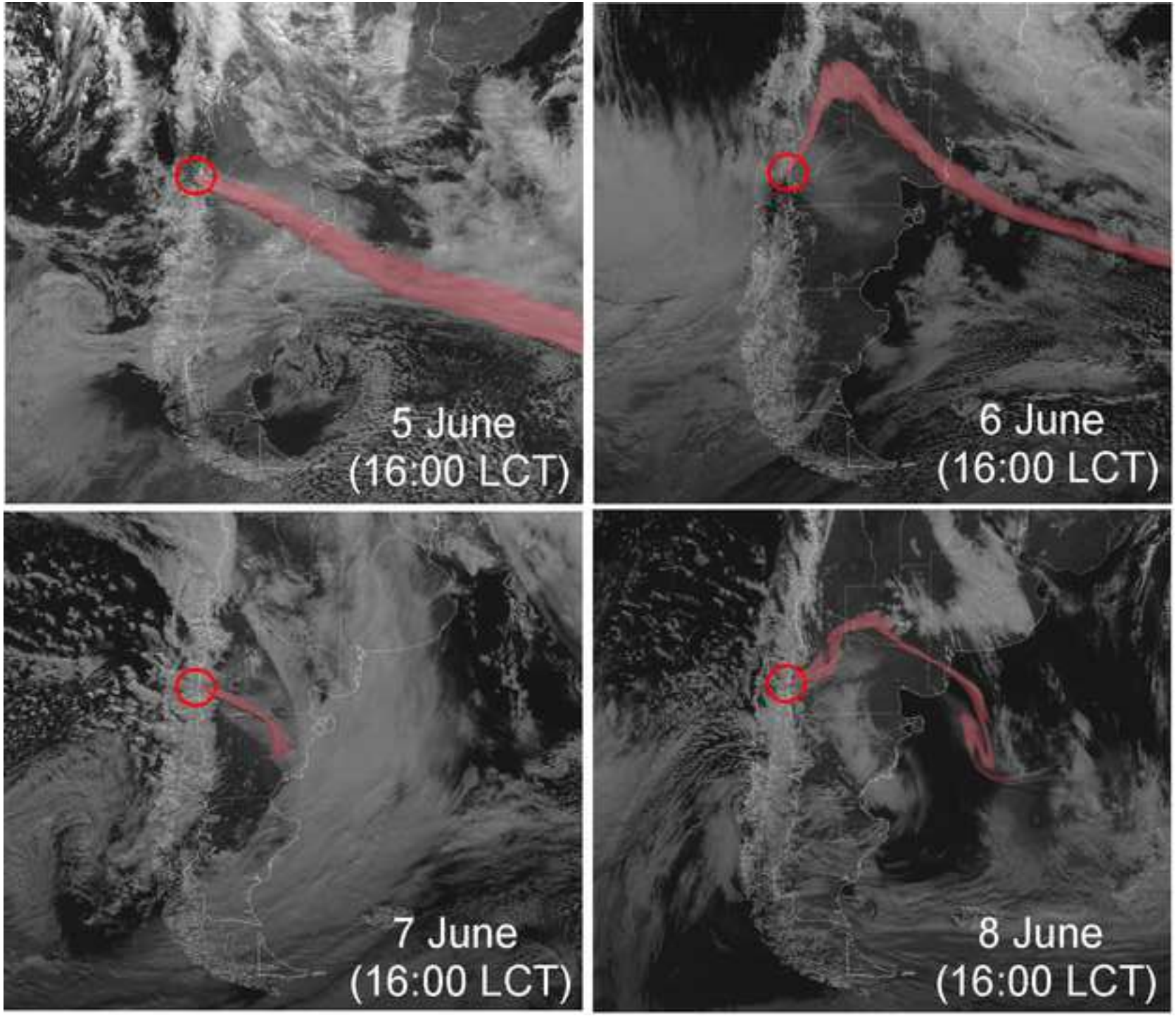

Figure 8
Click here to download high resolution image

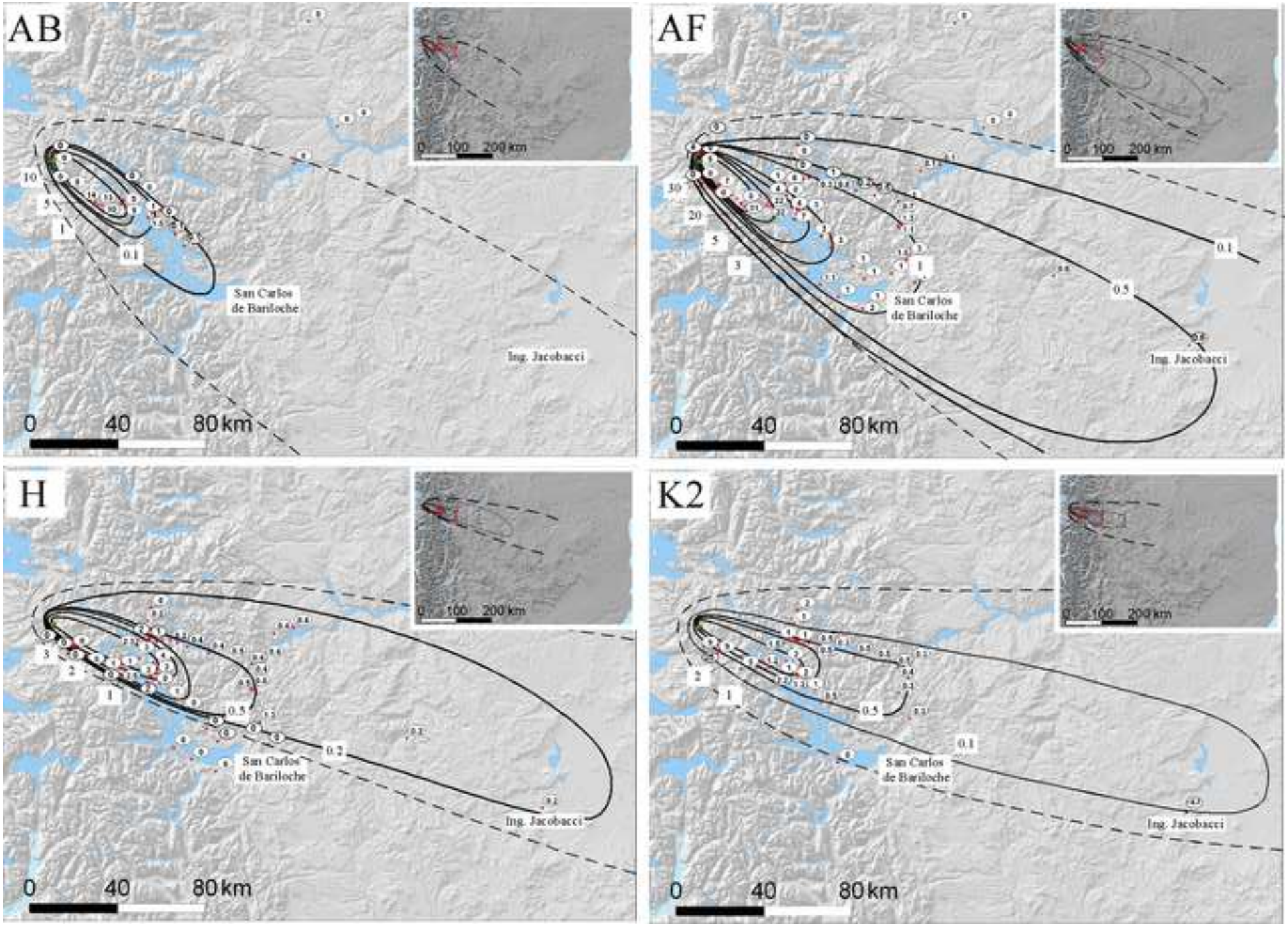

Figure 9
Click here to download high resolution image

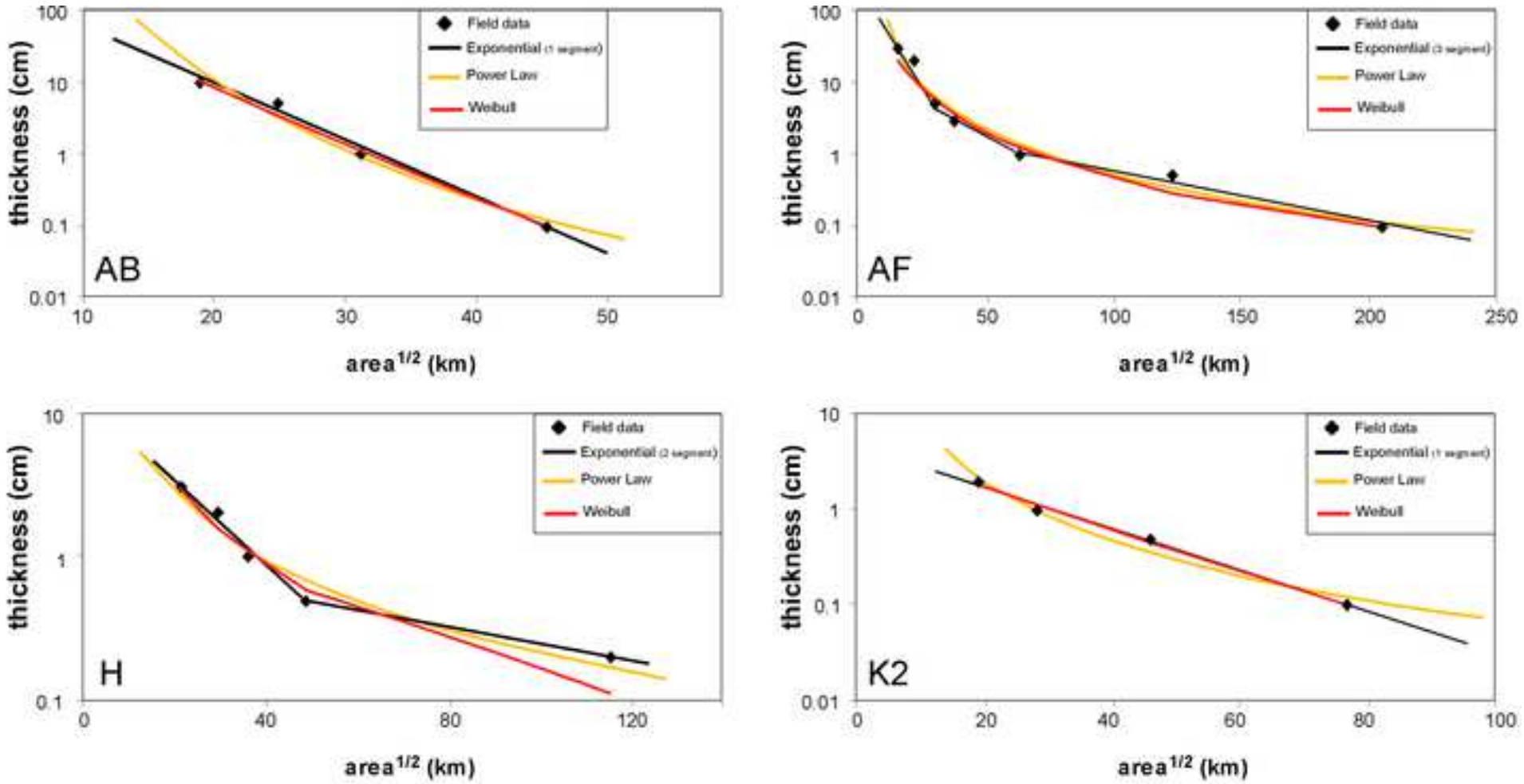

Figure 10

Click here to download high resolution image

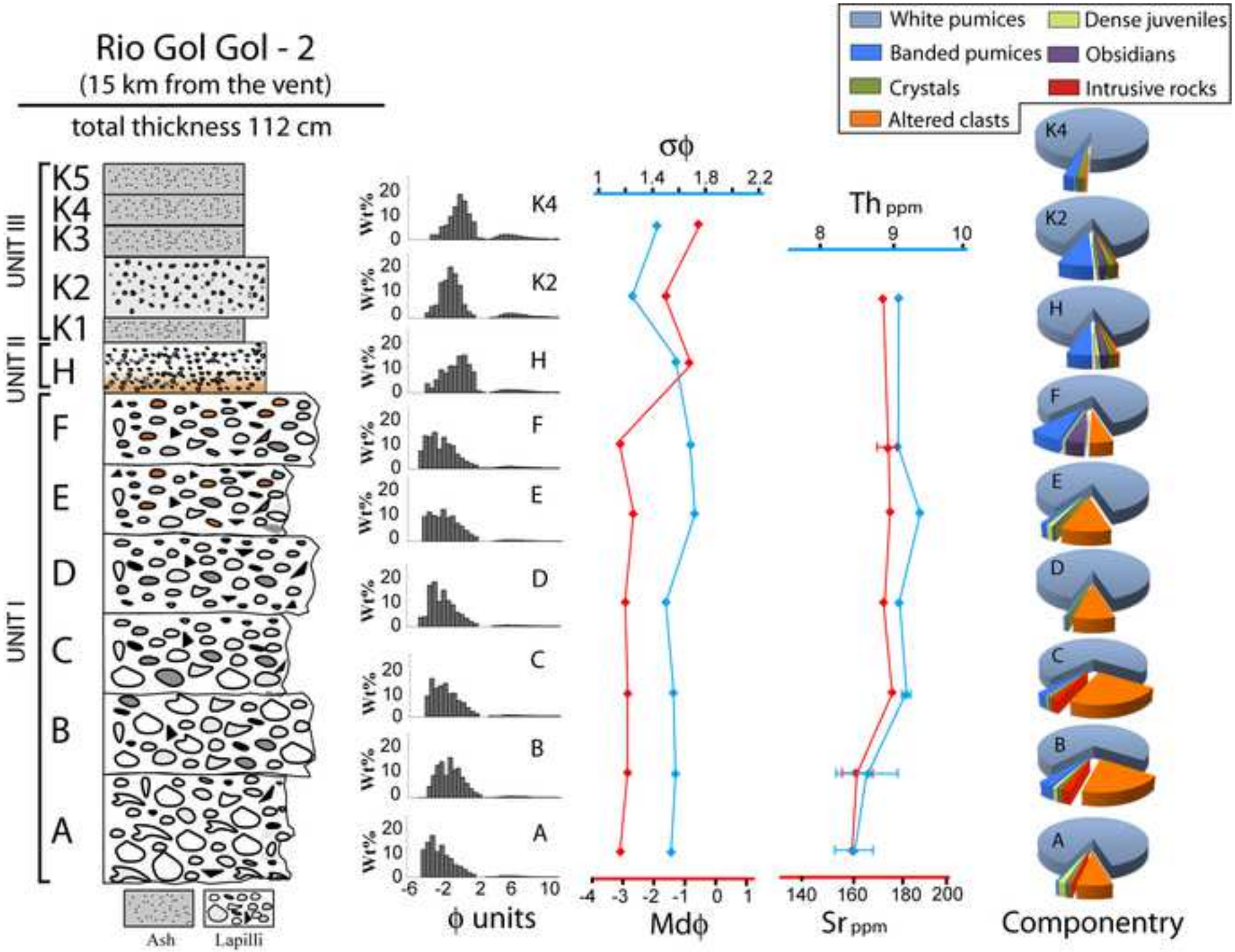

Figure 11
Click here to download high resolution image

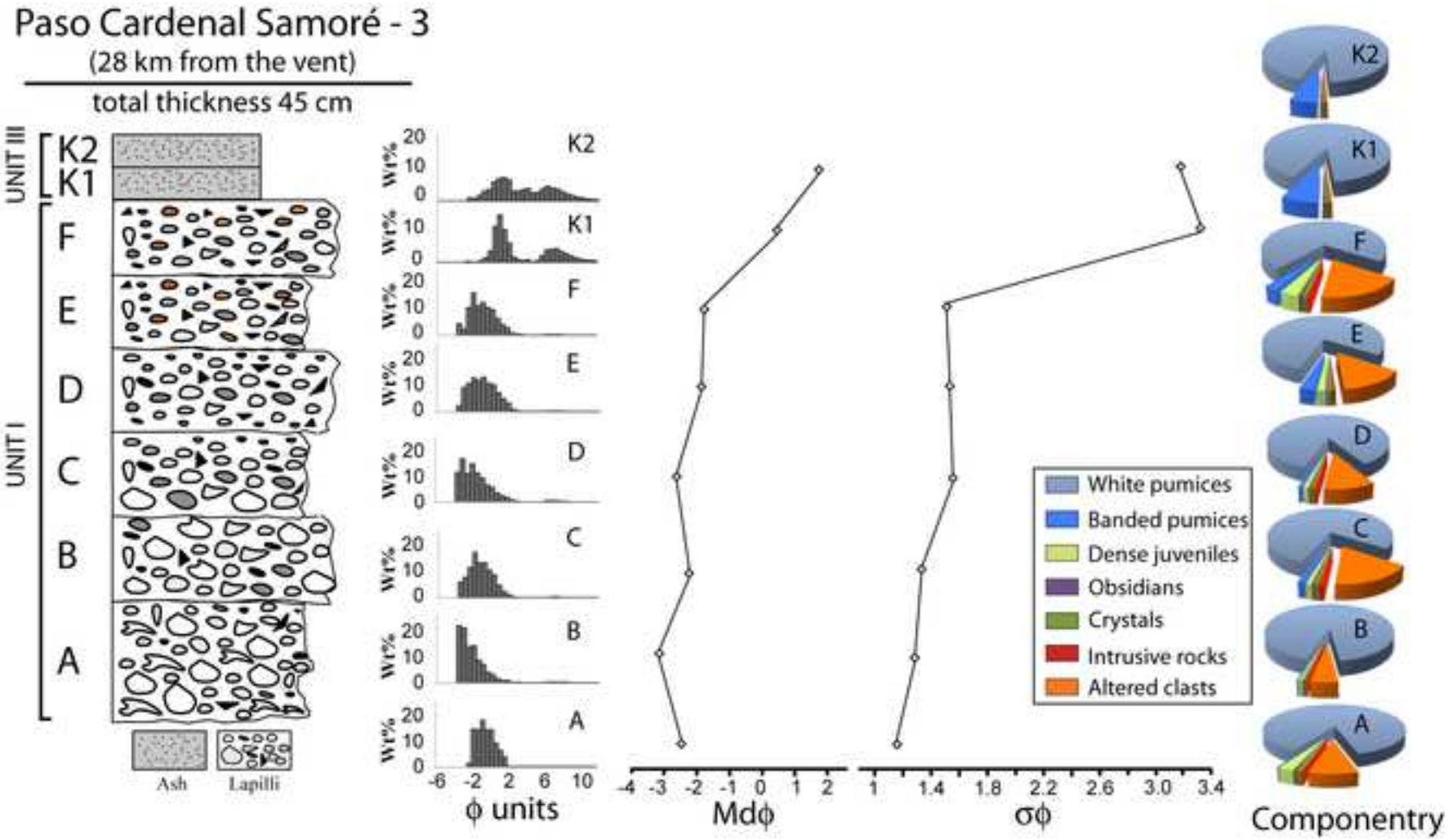

Figure 12
Click here to download high resolution image

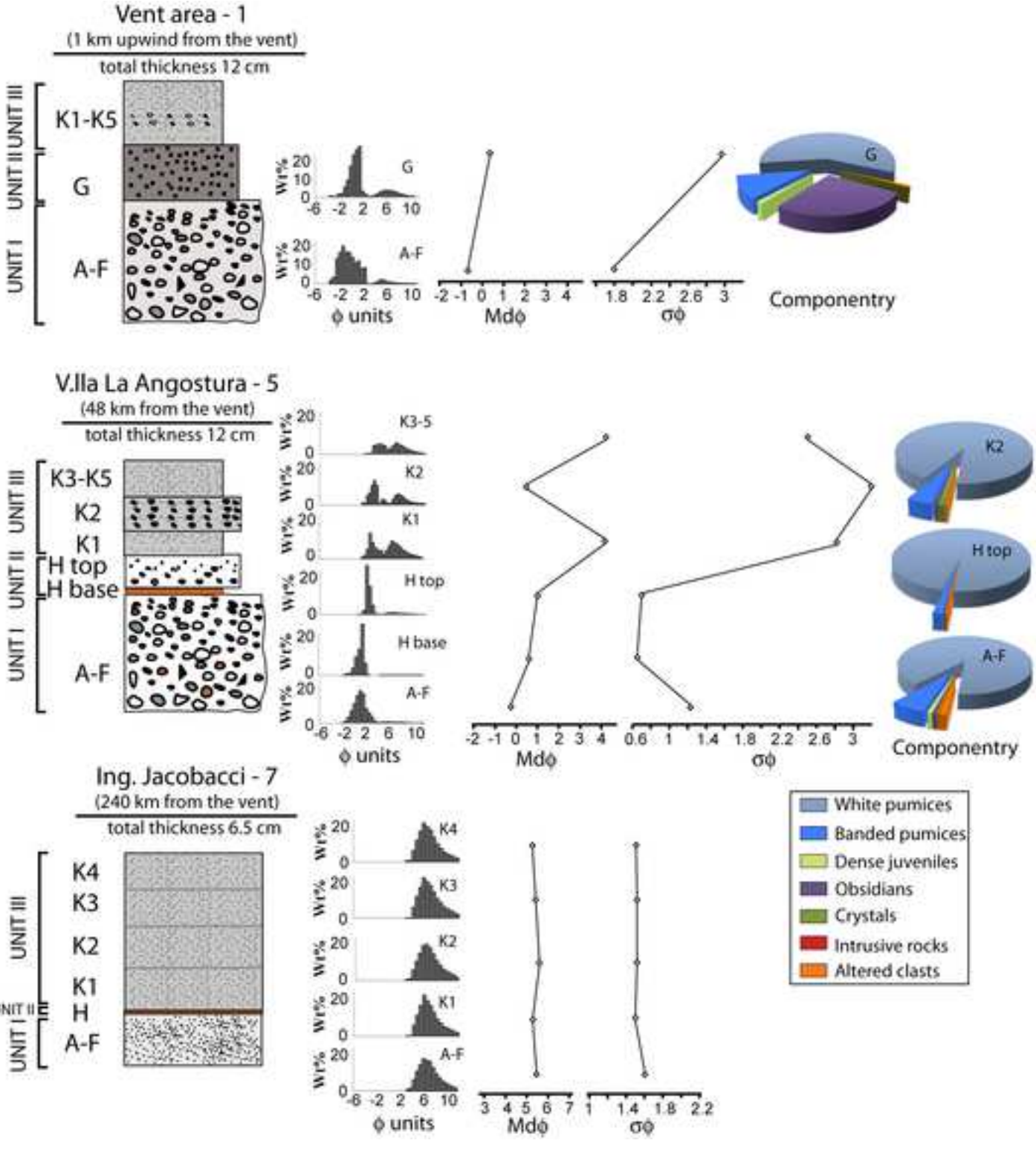

Figure 13
Click here to download high resolution image

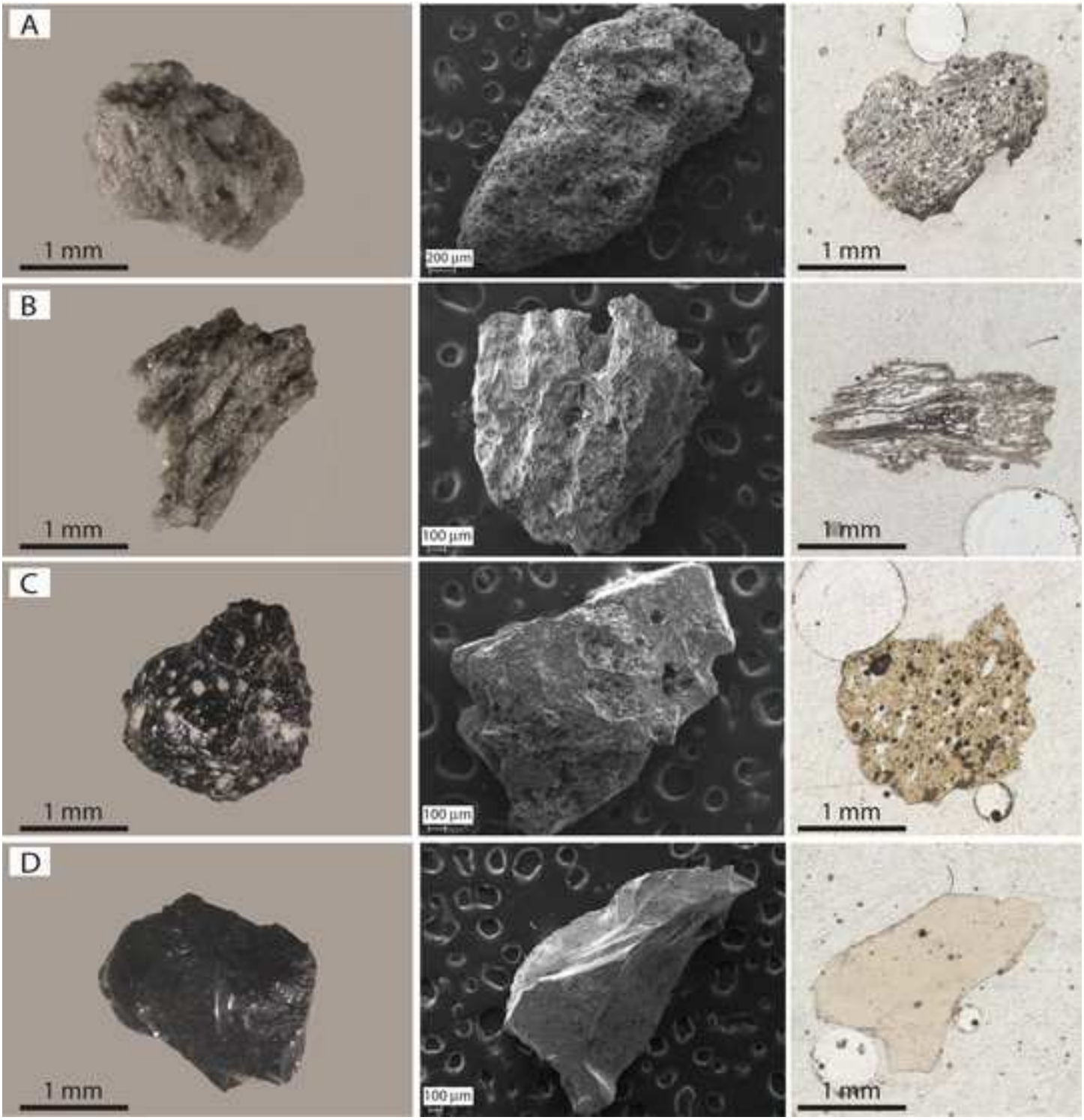

Figure 14
Click here to download high resolution image

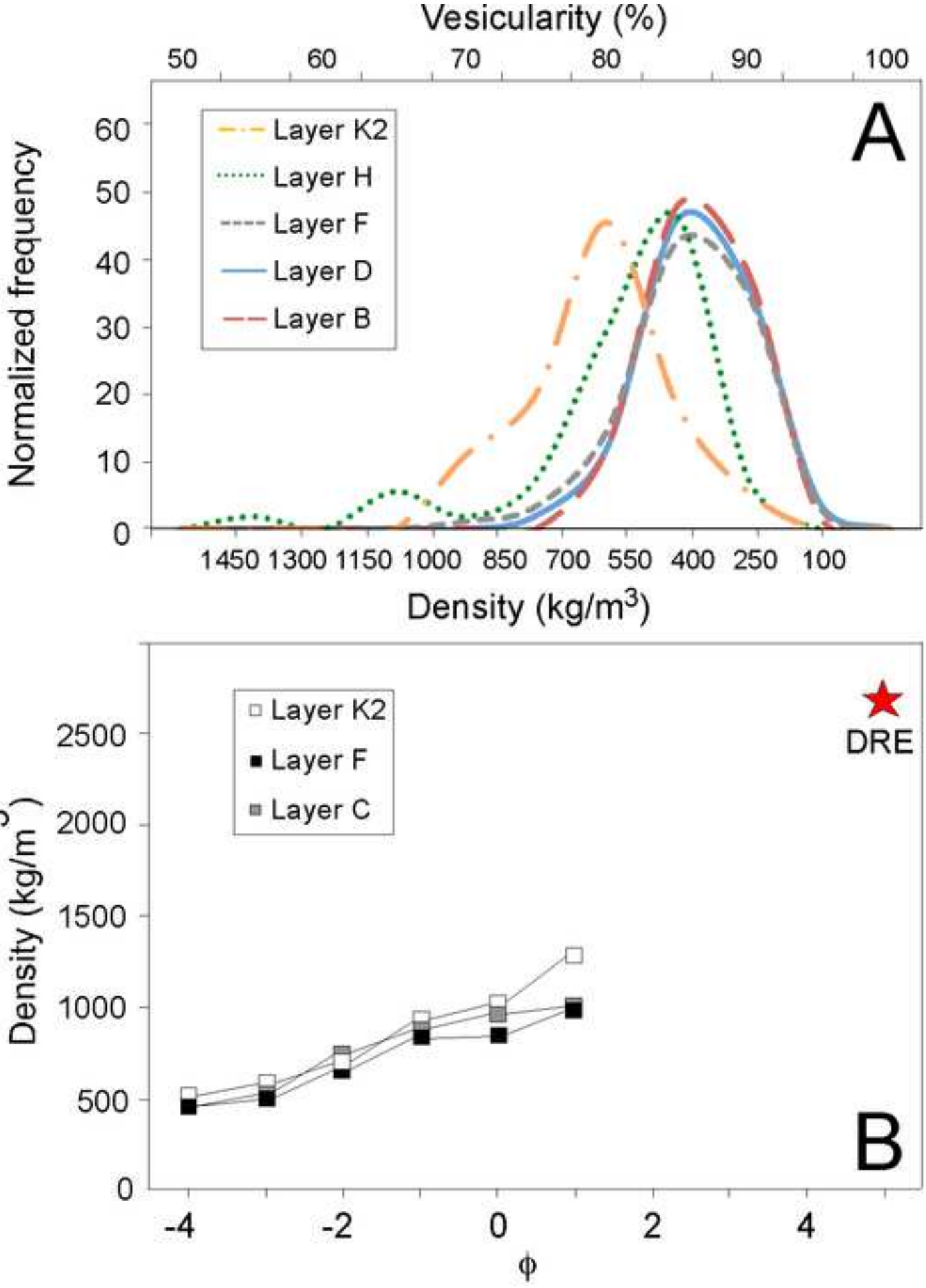

Figure 15
Click here to download high resolution image

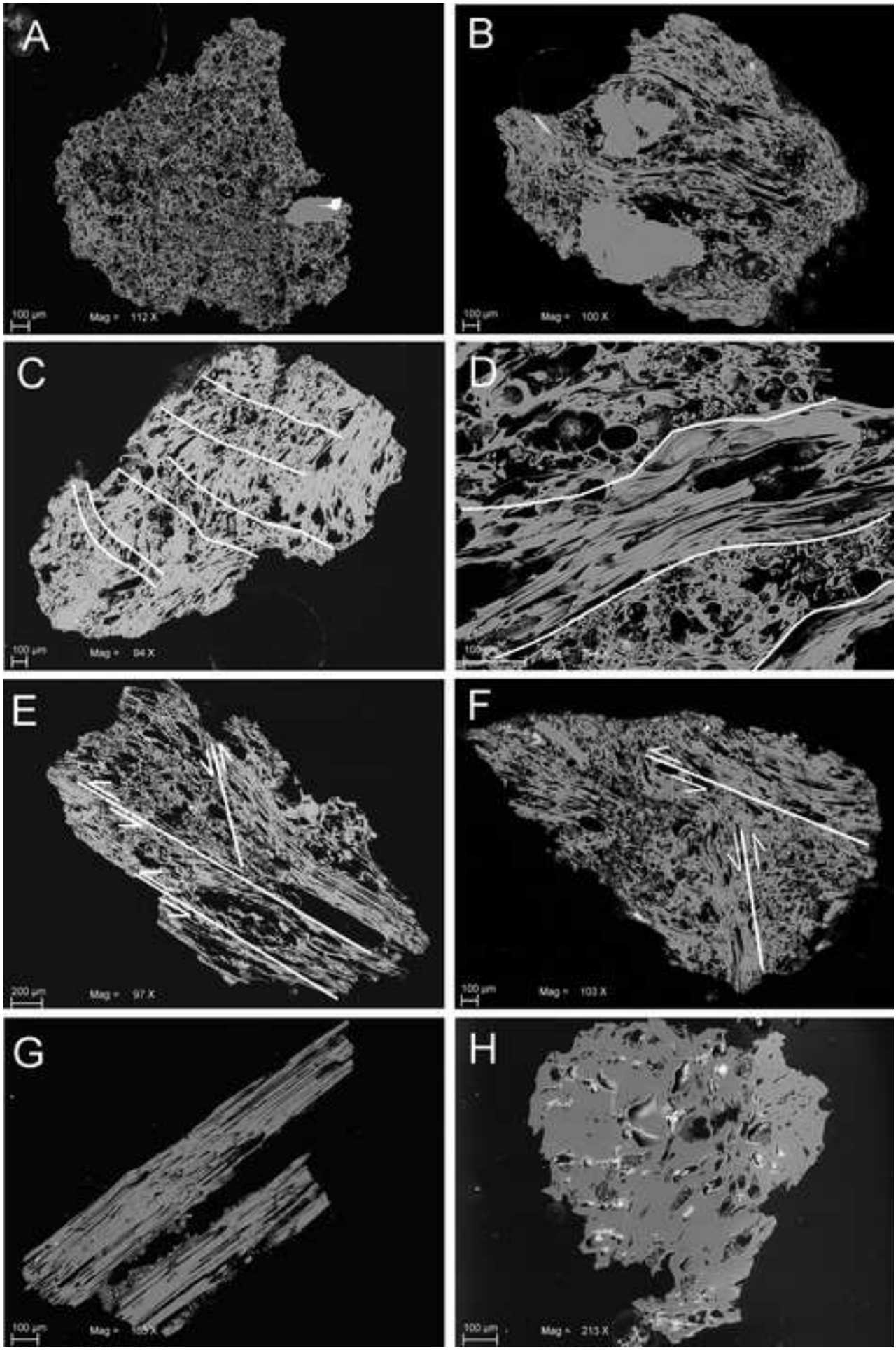

Table ESM1

Click here to download Supplementary Material: Table ESM1.docx

Table ESM2

Click here to download Supplementary Material: Table ESM2.docx